Monthly Notices
of the
ROYAL ASTRONOMICAL SOCIETY

MNRAS **481,** 2779–2803 (2018) doi:10.1093/mnras/sty2428
Advance Access publication 2018 September 5

An *INTEGRAL* overview of High-Mass X–ray Binaries: classes or transitions?

L. Sidoli ★ and A. Paizis
INAF, Istituto di Astrofisica Spaziale e Fisica Cosmica, Via E. Bassini 15, I-20133 Milano, Italy

Accepted 2018 August 30. Received 2018 August 22; in original form 2018 May 16

ABSTRACT

We analysed in a systematic way the public *INTEGRAL* observations spanning from December 2002 to September 2016, to investigate the hard X-ray properties of about 60 High Mass X-ray Binaries (HMXBs). We considered both persistent and transient sources, hosting either a Be star (Be/XRBs) or a blue supergiant companion (SgHMXBs, including Supergiant Fast X-ray Transients, SFXTs), a neutron star, or a black hole. *INTEGRAL* X-ray light curves (18–50 keV), sampled at a bin time of about 2 ks, were extracted for all HMXBs to derive the cumulative distribution of their hard X-ray luminosity, their duty cycle, and the range of variability of their hard X-ray luminosity. This allowed us to obtain an overall and quantitative characterization of the long-term hard X–ray activity of the HMXBs in our sample. Putting the phenomenology observed with *INTEGRAL* into context with other known source properties (e.g. orbital parameters, pulsar spin periods, etc.) together with observational constraints coming from softer X-rays (1–10 keV), enabled the investigation of the way the different HMXB sub-classes behave (and sometimes overlap). For given source properties, the different sub-classes of massive binaries seem to cluster in a suggestive way. However, for what concerns supergiant systems (SgHMXBs versus SFXTs), several sources with intermediate properties exist, suggesting a smooth transition between the two sub-classes.

Key words: accretion – stars: neutron – X–rays: binaries – X–rays.

1 INTRODUCTION

In recent years, the field of High-Mass X-ray Binaries (HMXBs) revitalized thanks to the discoveries performed by the INTErnational Gamma-Ray Astrophysics Laboratory (*INTEGRAL*; Winkler et al. 2003, 2011). The number of HMXBs with supergiant companions tripled (Krivonos et al. 2012; Bird et al. 2016) and new sub-classes of massive X–ray binaries were discovered: the so-called 'highly obscured sources' (the first was IGR J16318–4545, Courvoisier et al. 2003) and the Supergiant Fast X–ray Transients (SFXTs; Sguera et al. 2005; Negueruela et al. 2006), a new sub-class of transient X–ray sources associated with early-type supergiant stars. This latter new type of X–ray binaries (XRB) in particular, with its bright and short flaring emission, posed into question the standard picture of X–ray emission in supergiant HMXBs: Bondi–Hoyle accretion onto the neutron star (NS) of matter gravitationally captured from the wind of the massive donor. Many physical mechanisms were proposed to explain the SFXT X-ray flares: gated mechanisms (magnetic or centrifugal barriers; Grebenev & Sunyaev 2007; Bozzo, Falanga & Stella 2008) that halt the accretion most of the time (depending on the values of the NS spin period and surface magnetic field), or the quasi-spherical settling accretion regime, where the phenomenology of persistent supergiant HMXBs versus SFXTs is explained by different cooling regimes of the gravitationally captured matter above the NS magnetosphere (Shakura et al. 2012, 2014; Shakura & Postnov 2017). The characteristics of the (clumpy) wind from the companion are expected to play a fundamental role, acting as an external condition for the accreting pulsar. However, the properties of the companion wind (clump density, velocity, and magnetic field) are largely unknown in HMXBs (see Martínez-Núñez et al. 2017 for a comprehensive review of the supergiant winds and their impact onto the accretion in HMXBs hosting NSs).

A huge observational effort towards both the donor star and the X-ray source has been pushed forward in the recent years by many authors on specific interesting sources (see Sidoli 2017 for a review and references therein). A few years ago, we performed a systematic analysis of all publicly available *INTEGRAL* observations of all known SFXTs (Paizis & Sidoli 2014), compared with three classical persistent HMXBs. We found that the cumulative luminosity distributions of the SFXT X-ray flares were power-law-like, while the luminosity distributions of the three persistent HMXBs were more appropriately represented by log-normal functions. This suggests a different approach in obtaining observational information about the accretion mechanism and the production of the X-ray flares in

★ E-mail: sidoli@lambrate.inaf.it

SFXTs (Paizis & Sidoli 2014; Shakura et al. 2014; Sidoli et al. 2016).

In this work, we widen our investigation to all HMXBs observed by *INTEGRAL* in 14 years, to obtain a global view of all sub-classes of HMXBs in accretion (gamma-ray binaries and colliding-wind massive binaries are excluded). We report here a full characterization of their hard X-ray phenomenology by means of time-integrated quantities, insensitive to the temporal evolution of their long-term X-ray light curves. The extraction of cumulative luminosity distributions in the 18–50 keV energy range allows us to obtain quantitative information that offers a comprehensive picture of their behaviour at high energy, also put into context of other source properties.

The *paper* is structured as follows: in Section 2, we outline the *INTEGRAL* archive, the data analysis, and the selection of our sample of HMXBs; in Section 3, we report on our *INTEGRAL* results, the cumulative luminosity distributions, and the source duty cycles; in Section 4, we describe the search through the literature of other interesting properties for all members of our sample, producing an updated catalogue for the HMXBs of our interest; in Section 5, we discuss the results on both the cumulative luminosity distributions and the hard X–ray results into context of published properties. Our conclusions are given in Section 6.

2 *INTEGRAL*: DATA ANALYSIS AND THE SELECTION OF THE HMXB SAMPLE

INTEGRAL (Winkler et al. 2003, 2011) is a medium-size ESA mission launched in October 2002. It comprises two main gamma-ray instruments – the spectrometer SPI (15 keV – 10 MeV Vedrenne et al. 2003) and the imager IBIS (Ubertini et al. 2003) – two X–ray monitors, JEM–X (4–35 keV, Lund et al. 2003) and an optical camera, OMC (500–600 nm, Mas-Hesse et al. 2003). The imager IBIS consists of two layers, IBIS/ISGRI (15 keV – 1 MeV, Lebrun et al. 2003) and IBIS/PICsIT (0.175–10 MeV, Labanti et al. 2003).

The long-standing activity of *INTEGRAL*, its wide field of view (hereafter, FoV, 30°x30° for the imager) together with the good angular resolution in hard X-rays, essential in the crowded Galactic Plane and Centre regions, make *INTEGRAL* a very powerful instrument to study the wide sample of hard X-ray sources as a class.

2.1 The *INTEGRAL* archive

We have built an *INTEGRAL* archive, described in detail in Paizis et al. (2013), providing scientific results for IBIS/ISGRI public data. The scripts used to build the archive are online. [1] This database approach enabled an easy access to the long-term behaviour of a large sample of sources in the hard X-ray range, allowing us to explore the properties of a few members of the class of HMXBs, e.g. Paizis & Sidoli (2014), Sidoli et al. (2015); Sidoli, Paizis & Postnov (2016), Shakura et al. (2014), and Shakura et al. (2015). We investigate here a much larger sample of data and of HMXBs observed by *INTEGRAL*(see below for the selection of the sample).

We have recently developed a second generation archive, named ANITA (A New InTegral Archive), with important improved hardware and software issues/performances. Details of ANITA are given in Paizis et al. (2016) and in Paizis et al. (in prep.). For completeness, we recall here only the basic information relative to the results used in this work.

[1] http://www.iasf-milano.inaf.it/~ada/GOLIA.html

The public data analysed span a period of 14 years (December 2002–September 2016, revolution 0026 to 1729), for a total of ∼130 000 Science Windows (pointings, hereafter ScW, with a duration of ∼2 ks each). This corresponds to a total exposure time of ∼200 Ms. The standard *INTEGRAL* Off-line Scientific Analysis (OSA) version 10.2 software package has been used for the data analysis. For each ScW, images together with the list of detected sources are created in four energy bands: 18–50, 50–100, 100–150, 22–50 keV. Hereafter, we focus only on the results obtained in the 18–50 keV energy band that, notwithstanding the degradation of the low energy threshold of IBIS/ISGRI with time, provides the best detection statistics among all the aforementioned energy bands. The 22–50 keV band provides consistent results/trends with what is shown here. In this work, ScWs with durations smaller than 1 ks have been ignored, to avoid non-standard snapshot contaminations. Furthermore, only ScWs with the sources within 12° from the centre of the FoV have been considered.

Our selection (ScW exposure >1 ks and off axis angle <12°) provides the source final *field exposure*. Within this field exposure, a source is considered detected, i.e. *active* at the ScW level in the 18–50 keV band, when the detection significance is higher than 5 sigma in the ScW. We thus obtain the source duty cycle, $DC_{18-50\,keV}$, as the per centage of detections at ScW level: activity time over field exposure time. The HMXBs that have been detected (i.e. are active) at ScW level are the object of this work. For each source in our sample, we list in Table 1 the *INTEGRAL field exposure* (in units of seconds; col. 2), the *source activity* (col. 3) and the source $DC_{18-50\,keV}$ in the energy range 18–50 keV (col. 4).

INTEGRAL has performed a very thorough coverage of the Galactic plane where HMXBs reside and the selected <12° radius region results in a wide serendipitous source activity sampling. Indeed, unless an external bias is introduced, the sources will display a given flux regardless of their position in the FoV. However, there are some important aspects that need to be taken into account. First of all, we note that using only the fully coded FoV (source $\lesssim$5° from the centre, where the sensitivity is maximal and approximately constant) results in a much smaller data sample, wasting an important fraction of the FoV coverage. Furthermore, it introduces an important bias in the $DC_{18-50\,keV}$ estimation: Be X–ray Transients (Be/XRTs, hereafter), for which several target of opportunities (ToOs) have been performed, ending up with a much higher $DC_{18-50\,keV}$ when only a small portion of the FoV is considered. This is because ToOs are on-source observations. We note that no ToO observation has ever been performed on SFXTs except one, on IGR J11215-5952, during which the source was not detected (Sidoli et al. 2007). Indeed, the SFXT flares detectable by IBIS/ISGRI are typically shorter than the ToO reaction time of the satellite. In a similar way, phase-resolved observations, and in general time-constrained ones, provide an artificially high $DC_{18-50\,keV}$ when only the fully coded FoV is considered. These aspects are clearly mitigated using a larger portion of the FoV. This effect is maximum in the case of three Be/XRTs (H 0115 + 634, EXO 0331 + 530 and 1A 0535 + 262) that have been the target of several ToOs. Indeed, for these sources, the $DC_{18-50\,keV}$ decreases, respectively, from about 37 per cent, 56 per cent, and 25 per cent when the 5° fully coded FoV is considered, to 10 per cent, 25 per cent, and 12 per cent when the region up to 12° is included. Hence, while moving from the on-target ToO observations (with the source in the fully coded FoV) to the partially coded FoV (that includes serendipitous observations) the overall $DC_{18-50\,keV}$ decreases. This does not mean that the bias introduced by the on-target ToO observations is completely eliminated using a 12° radius selection, but it is highly diluted: indeed,

Table 1. *INTEGRAL* IBIS/ISGRI results (18–50 keV) for our sample of HMXBs.

Name[a]	Field exposure (s)	Source activity (s)	Duty Cycle (per cent)	Average L_X (erg s^{-1})	Min L_X (erg s^{-1})	Max L_X (erg s^{-1})	Dynamic range Max L_X / Min L_X
			SgHMXBs				
SMC X-1∗	3.7E+06	1.8E+06	49.05	1.7E+38	7.0E+37	3.0E+38	4.25
3A 0114+650	7.0E+06	1.0E+06	14.63	2.1E+36	6.7E+35	1.2E+37	17.31
Vela X-1∗	5.2E+06	4.1E+06	79.22	1.3E+36	6.1E+34	1.0E+37	165.74
1E 1145.1-6141	6.4E+06	2.0E+06	31.95	3.0E+36	1.0E+36	1.4E+37	13.86
GX 301-2	6.2E+06	5.8E+06	94.47	2.8E+36	2.3E+35	3.0E+37	127.46
H 1538-522∗	8.4E+06	2.5E+06	30.15	9.2E+35	4.2E+35	4.3E+36	10.19
IGR J16207-5129	9.2E+06	3.6E+04	0.39	1.1E+36	6.5E+35	2.1E+36	3.24
IGR J16320-4751	1.0E+07	2.2E+06	21.32	5.9E+35	1.8E+35	2.5E+36	14.01
IGR J16393-4643	1.1E+07	4.2E+04	0.40	3.4E+36	1.5E+36	6.2E+36	4.02
OAO 1657-415∗	1.2E+07	7.3E+06	59.78	5.8E+36	1.0E+36	2.0E+37	19.04
4U 1700-377∗	1.6E+07	1.2E+07	73.09	1.1E+36	8.5E+34	9.5E+36	111.43
IGR J17252-3616∗	2.3E+07	1.1E+06	4.65	2.9E+36	1.3E+36	9.5E+36	7.34
IGR J18027-2016∗	2.1E+07	1.1E+05	0.54	5.2E+36	2.7E+36	1.3E+37	4.92
IGR J18214-1318	8.9E+06	5.7E+03	0.06	3.4E+36	2.0E+36	5.1E+36	2.60
XTE J1855-026∗	8.4E+06	8.1E+05	9.64	4.2E+36	2.1E+36	1.9E+37	9.05
H 1907+097	8.7E+06	1.8E+06	20.13	8.1E+35	3.6E+35	4.8E+36	13.48
4U 1909+07	8.7E+06	2.2E+06	24.84	7.1E+35	3.5E+35	3.5E+36	9.96
IGR J19140+0951	8.8E+06	1.2E+06	14.18	5.2E+35	2.0E+35	3.3E+36	16.36
			giant HMXBs				
LMC X-4∗	7.8E+06	3.7E+06	47.23	1.2E+38	4.4E+37	2.3E+38	5.11
Cen X-3∗	6.1E+06	3.8E+06	62.79	4.0E+36	5.8E+35	1.4E+37	24.34
			SFXTs				
IGR J08408-4503	5.4E+06	4.9E+03	0.09	3.0E+35	2.7E+35	3.4E+35	1.27
IGR J11215-5952	6.0E+06	3.9E+04	0.64	1.6E+36	8.6E+35	5.1E+36	5.92
IGR J16328-4726	1.0E+07	2.9E+04	0.28	1.7E+36	7.9E+35	3.6E+36	4.56
IGR J16418-4532∗	1.1E+07	1.3E+05	1.22	6.1E+36	3.0E+36	2.1E+37	7.07
IGR J16465-4507	1.1E+07	1.9E+04	0.18	2.9E+36	2.1E+36	4.9E+36	2.29
IGR J16479-4514∗	1.1E+07	3.6E+05	3.33	3.6E+35	1.6E+35	1.2E+36	7.47
IGR J17354-3255	2.5E+07	3.5E+03	0.01	3.0E+36	1.9E+36	4.6E+36	2.38
XTE J1739-302	2.5E+07	2.2E+05	0.89	4.8E+35	1.5E+35	1.5E+36	9.78
IGR J17544-2619	2.5E+07	1.3E+05	0.54	5.6E+35	2.0E+35	5.3E+36	25.99
SAX J1818.6-1703	1.1E+07	9.1E+04	0.81	2.9E+35	1.1E+35	1.4E+36	12.24
IGR J18410-0535	7.9E+06	4.2E+04	0.53	3.8E+35	2.2E+35	8.5E+35	3.87
IGR J18450-0435	8.0E+06	2.8E+04	0.35	1.5E+36	1.0E+36	2.7E+36	2.57
IGR J18483-0311	8.2E+06	3.8E+05	4.63	5.2E+35	2.3E+35	1.5E+36	6.63
			Be/XRBs				
H 0115+634	7.1E+06	6.8E+05	9.55	1.5E+37	9.9E+35	3.7E+37	36.90
RX J0146.9+6121	4.7E+06	5.0E+03	0.11	1.1E+35	1.0E+35	1.1E+35	1.11
EXO 0331+530	2.8E+06	7.1E+05	25.10	2.4E+37	9.4E+35	6.4E+37	68.01
X Per	2.1E+06	1.6E+06	76.96	2.5E+34	1.2E+34	6.3E+34	5.19
1A 0535+262	7.2E+06	8.9E+05	12.34	4.4E+36	9.9E+34	1.5E+37	153.68
GRO J1008-57	4.8E+06	4.3E+05	8.87	2.4E+36	5.6E+35	9.8E+36	17.68
4U 1036-56	5.1E+06	1.8E+04	0.35	7.5E+35	5.2E+35	9.9E+35	1.88
IGR J11305-6256	6.3E+06	2.5E+04	0.41	1.9E+35	1.3E+35	3.0E+35	2.30
IGR J11435-6109	6.4E+06	1.7E+05	2.68	1.4E+36	9.9E+35	2.1E+36	2.08
H 1145-619	6.3E+06	6.8E+04	1.07	1.2E+35	8.1E+34	1.9E+35	2.34
XTE J1543-568	7.0E+06	9.9E+03	0.14	2.7E+36	2.1E+36	3.3E+36	1.58
AX J1749.1-2733	2.5E+07	4.2E+04	0.17	8.1E+36	4.1E+36	1.3E+37	3.11
GRO J1750-27	2.5E+07	1.2E+06	4.88	2.9E+37	7.8E+36	8.5E+37	10.95
AX J1820.5-1434	9.5E+06	1.4E+04	0.15	2.1E+36	1.7E+36	3.8E+36	2.24
Ginga 1843+009	9.3E+06	3.2E+05	3.39	5.8E+36	1.5E+36	1.6E+37	10.33
XTE J1858+034	1.0E+07	5.3E+05	5.34	8.8E+36	1.7E+36	1.5E+37	8.91
4U 1901+03	9.9E+06	1.0E+06	10.44	1.2E+37	2.7E+36	1.9E+37	6.81
KS 1947+300	9.9E+06	9.3E+05	9.41	6.8E+36	1.7E+36	1.7E+37	10.20
EXO 2030+375	1.2E+07	3.5E+06	28.99	7.8E+36	9.2E+35	6.4E+37	69.34
SAX J2103.5+4545	8.1E+06	9.0E+05	11.14	2.0E+36	7.5E+35	8.4E+36	11.23
			Other HMXBs				
IGR J16318-4848	9.9E+06	3.5E+06	35.17	7.4E+35	2.2E+35	4.1E+36	18.73
3A 2206+543	4.7E+06	3.0E+05	6.41	2.5E+35	1.3E+35	6.7E+35	4.99

Table 1 – *continued*

Name[a]	Field exposure (s)	Source activity (s)	Duty Cycle (per cent)	Average L_X (erg s^{-1})	Min L_X (erg s^{-1})	Max L_X (erg s^{-1})	Dynamic range Max L_X / Min L_X
Cyg X-1	1.1E+07	1.1E+07	99.88	2.5E+36	9.1E+34	8.2E+36	89.51
Cyg X-3	1.2E+07	1.1E+07	93.49	1.0E+37	1.3E+36	2.5E+37	19.82
SS 433∗	9.2E+06	1.4E+06	14.97	8.5E+35	4.5E+35	1.9E+36	4.25
			Symbiotic binary				
XTE J1743-363	2.4E+07	3.1E+04	0.13	1.1E+36	9.2E+35	1.5E+36	1.62

Note. [a]Sources marked with an asterisk are eclipsing binaries.

a large serendipitous coverage area is included in the duty cycle estimate. Unfortunately, a bigger fraction of the IBIS/ISGRI detector cannot be considered: the usage of the whole FoV would result in a $DC_{18-50\,keV}$ of about 8 per cent, 19 per cent, and 12 per cent for the three sources, respectively, but the (noisy) outer regions of the detector ($>12^\circ$) produce spurious detections, hence these latter per centages are highly unreliable.

On the other side, the inclusion of a portion of the partially coded FoV ($>5^\circ$, where the sensitivity decreases towards the instrumental edge) includes a detection bias in the sources that emit mostly at the IBIS/ISGRI detection threshold. Indeed, a – constant – source that is detected at 5 sigma in the totally coded FoV will be undetected in the partially coded FoV (the further out, the lower the detection significance). We have seen, however, that with our choice of FoV ($<12^\circ$) this bias is important only for three sources: X Per (a Be/XRB that is seen as a persistent source given its proximity – 0.8 kpc), H 1538-522 (SgHMXB), and 1E 1145.1-6141 (SgHMXB). Indeed, in these sources, the $DC_{18-50\,keV}$ shifts dramatically to lower values when a radius of 12° is considered. For example X Per would have a $DC_{18-50\,keV}$ ∼90 instead of ∼77 per cent if only data $<5^\circ$ were to be considered. Similarly, for the case of H 1538-522 and 1E 1145.1-6141. Hence, we may be losing detections and in reality these sources may be more persistent than what are considered here. However, as it will appear clear throughout the text, this has no influence on our conclusions: notwithstanding the detection loss, the sources are already amongst the ones with the highest $DC_{18-50\,keV}$ and their shift towards even higher DC values does not change our final considerations. For the remaining sources of the sample, this bias has no effect, i.e. when active, the sources are bright enough to be detected within 12° from the centre.

Finally, in order to quantify the effect of the IBIS/ISGRI degradation throughout the years, the overall Crab results will also be shown. In this respect, the Crab can be considered as the 'point spread function' of our results.

We believe that our selection criteria are the best trade-off currently available to maximize the scientific output of the *INTEGRAL* archive, while minimizing observational biases.

2.2 The HMXB sample

Given our detection criteria (ScW exposure >1 ks, off axis angle $<12^\circ$ and ScW detection $\geqq$5 sigma), we obtain a sample of 58 HMXBs (plus one symbiotic X–ray transient, XTE J1743-363). All but two (LMC X–4 and SMC X-1) are Galactic sources, that represent about half of the total number of HMXBs known in our Galaxy (Liu et al. 2006). They belong to different sub-classes: persistent HMXBs with supergiant companions (SgHMXBs, hereafter); HMXBs with early-type giant donor stars (Roche lobe overflow systems, like Cen X–3 and LMC X–4); the Supergiant Fast X–ray Transients (SFXTs); Be X–ray binaries (hereafter Be/XRBs, meant to include both persistent and transient Be sources – in case we only mean the X–ray transient Be systems, we will use the acronym Be/XRTs); black-hole binaries and other peculiar sources (Cyg X–1, Cyg X–3, SS 433); the source 3A 2206+543 (where the companion has an anomalous wind, Blay, Ribó & Negueruela 2009); the highly obscured source IGR J16318–4848 (Courvoisier et al. 2003), where the companion is a B[e] supergiant star (Filliatre & Chaty 2004; Chaty & Rahoui 2012), that is a supergiant star that shows the B[e] phenomenon (forbidden emission lines in its optical spectrum, Lamers et al. 1998). Finally, our sample includes also a symbiotic X–ray transient, XTE J1743–363 (Bozzo et al. 2013), where a compact object accretes matter from the wind of an M8 III giant, in order to compare its behaviour with other wind-fed massive X–ray binaries with OB-type stars, from the point of view of its hard X–ray emission.

3 *INTEGRAL* RESULTS

Table 1 summarizes our IBIS/ISGRI results (see Section 2.1 for the definition of the columns).

3.1 From count-rate to luminosity

Conversion factors from IBIS/ISGRI count-rates to X–ray luminosities (18–50 keV) have been derived from the analysis of IBIS/ISGRI spectra extracted from a subsample of HMXBs, fitted with models typical for accreting pulsars, like power laws with high energy cutoff. The subsample adopted for the IBIS/ISGRI spectroscopy included the following sources: Vela X-1, 4U 1700-377, H 1907+097, IGR J08408-4503, IGR J11215-5952, IGR J16418-4532, IGR J16465-4507, IGR J16479-4514, XTE J1739-302, IGR J17544-2619, SAX J1818.6-1703, IGR J18410-0535, IGR J18450-0435, and IGR J18483-0311. For each source, we extracted an average spectrum from a subsample of ScWs where the sources were detected above 5 sigma, within 12° from the FoV centre. We verified that within the considered observations no strong evidence for spectral variability was present. For each source, we fitted the average spectra in XSPEC using power law models with exponential cutoffs (CUTOFFPL or POW*HIGHECUT models in XSPEC). From this spectroscopy, we derived an average conversion factor of 4.5×10^{-11} erg cm^{-2} $count^{-1}$ to obtain the source fluxes. Source distances listed in Table 2 were then used to calculate the luminosities in hard X–rays (18–50 keV).

For the Crab, that has a different spectrum and we consider as our standard candle to get an idea of the luminosity variability of the different sources, an average spectrum was extracted from a subsample of ScWs as well. Fitting it with a power law model, we obtained a conversion factor of 4.7×10^{-11} erg cm^{-2} $count^{-1}$ (18–50 keV). A distance of 2 kpc was adopted to obtain the luminosity.

Table 2. Summary of the source properties extracted from the literature for the different types of HMXBs of our sample.

Name	Dist (kpc)	P_{orb} (d)	ecc	P_{spin} (s)	F_{min} (1–10 keV) (erg cm^{-2} s^{-1})	F_{max} (1–10 keV) (erg cm^{-2} s^{-1})	$DR_{1-10\,keV}$ (F_{max}/F_{min})	References[a]
				SgHMXBs				
SMC X-1	61 ± 1	3.89	0.0002	0.71	2.80E-10	2.15E-09	7.7	14, 4, 4, 4, 7, 11
3A 0114+650	7.2 ± 3.6	11.60	0.18	10008	1.00E-10	–	–	1, 1, 4, 6, 12, –
Vela X-1	1.9 ± 0.2	8.96	0.09	283.5	7.50E-10	1.27E-09	1.7	7, 1, 5, 1, 7, 7
1E 1145.1-6141	8.5 ± 1.5	14.36	0.2	296.6	6.00E-11	–	–	1, 1, 4, 1, 13, –
GX 301-2	3.5 ± 0.5	41.49	0.46	675	1.20E-09	3.10E-09	2.6	1, 1, 4, 1, 7, 7
H 1538-522	5.0 ± 0.5	3.73	0.18	526.8	4.10E-12	1.35E-10	32.9	1, 1, 5, 1, 7, 7
IGR J16207-5129	6.0 ± 3.5	9.73	–	–	4.30E-12	4.00E-11	9.3	1, 1, –, –, 15, 16
IGR J16320-4751	3.5	8.99	–	1309	5.30E-11	7.80E-10	14.7	1, 1, –, 1, 7, 7
IGR J16393-4643	10.6	4.24	0.0[b]	912	2.80E-11	9.00E-11	3.2	18, 1, –, 1, 19, 20
OAO 1657-415	7.1 ± 1.3	10.45	0.103	38.2	8.00E-11	8.00E-10	10	21, 1, 5, 1, 6, 6
4U 1700-377	1.9 ± 0.3	3.41	0.0[b]	–	3.00E-10	3.60E-09	12.0	1, 1, –, –, 7, 7
IGR J17252-3616	8 ± 2	9.74	0.0	413.89	4.00E-12	6.90E-11	17.3	21, 1, 5, 1, 6, 7
IGR J18027-2016	12.4 ± 0.1	4.57	–	139.61	4.00E-12	1.50E-09	375	1, 5, –, 1, 22, 22
IGR J18214-1318	8 ± 2	–	–	–	5.80E-11	–	–	21, –, –, –, 23, –
XTE J1855-026	10.8 ± 1.0	6.07	0.04	360.7	1.10E-10	–	–	24, 1, 5, 1, 6, –
H 1907+097	5.0 ± 1.2	8.36	0.28	437.5	9.70E-12	5.30E-09	546	1, 1, 6, 1, 72, 6
4U 1909+07	4.85 ± 0.5	4.4	0.021	605	2.60E-10	3.00E-09	11.5	1, 1, 6, 1, 25, 26
IGR J19140+0951	3.6 ± 1.0	13.55	–	5900	2.60E-12	2.00E-09	769	27, 1, –, 28, 29, 30
				giant HMXBs				
LMC X-4	50 ± 1	1.4	0.006	13.5	7.40E-11	2.50E-10	3.4	68, 5, 5, 5, 12, 12
Cen X-3	6.5 ± 1.5	2.09	0.0[b]	4.82	4.40E-10	2.20E-09	5.0	3, 3, –, 3, 7, 69
				SFXTs				
IGR J08408-4503	2.7	9.54	0.63	–	4.00E-13	2.70E-09	6750	2, 2, 2, 2, 8, 9
IGR J11215-5952	7.0 ± 1.0	164.6	>0.8	187	<5.00E-13	2.40E-10	>480	2, 2, 2, 2, 10, 17
IGR J16328-4726	7.2 ± 0.3	10.07	–	–	5.00E-12	1.50E-09	300	2, 2, 2, 2, 31, 32
IGR J16418-4532	13	3.75	0.0	1212	6.50E-12	2.00E-09	308	2, 2, 2, 2, 33 , 32
IGR J16465-4507	9.5 ± 5.7	30.24	–	228	4.00E-12	1.50E-10	37.5	2, 2, 2, 2, 7, 32
IGR J16479-4514	2.8 ± 1.7	3.32	0.0	–	6.00E-12	1.00E-08	1667	2, 2, 2, 2, 34, 35
IGR J17354-3255	8.5	8.45	–	–	<1.40E-13	1.30E-10	>929	2, 2, 2, 2, 36, 37
XTE J1739-302	2.7	51.47	–	–	<2.50E-12	5.10E-09	>2040	2, 2, 2, 2, 32, 9
IGR J17544-2619	3.0 ± 0.2	4.93	<0.4	71.49(?)[b]	6.00E-14	1.00E-07	1.67×10^6	2, 2, 2, 2, 38, 39
SAX J1818.6-1703	2.1 ± 0.1	30	–	–	<1.10E-13	1.50E-10	>1364	2, 2, 2, 2, 40, 41
IGR J18410-0535	3 ± 2	6.45	–	–	9.00E-14	1.00E-09	1.1×10^4	2, 2, 2, 2, 42, 32
IGR J18450-0435	6.4	5.7	–	–	3.90E-12	2.00E-09	513	2, 2, 2, 2, 31, 32
IGR J18483-0311	3.5 ± 0.5	18.52	∼0.4	21.05	8.90E-13	8.00E-10	899	2, 2, 2, 2, 7, 32
				Be/XRBs				
H 0115+634	8 ± 1	24.32	0.34	3.61	2.80E-14	4.00E-09	1.4×10^5	43, 4, 4, 4, 12, 44
RX J0146.9+6121	2.3 ± 0.5	330	–	1400	1.70E-11	–	–	43, 43, 43, 43, 7, –
EXO 0331+530	7.0 ± 1.5	36.5	0.42	4.38	2.80E-14	3.00E-08	1.07×10^6	43, 4, 4, 4, 7, 45
X Per	0.8 ± 0.14	250	0.11	837.7	1.00E-10	1.00E-09	10	21, 4, 4, 4, 46, 46
1A 0535+262	2.0 ± 0.7	111	0.47	103.5	3.70E-12	1.00E-07	2.7×10^4	43, 43, 43, 4, 47
GRO J1008-57	5.8	249.48	0.68	93.5	2.21E-11	4.00E-09	181	48, 48, 48, 48, 56, 49
4U 1036-56	5	60.9	–	853.4	4.00E-12	2.40E-10	60	43, 50, –, 51, 52, 52
IGR J11305-6256	3	–	–	–	4.30E-11	–	–	3, 3, –, 3, 23, –
IGR J11435-6109	8 ± 2	52.4	–	161.76	8.30E-12	–	–	3, 3, –, 3, 23, –
H 1145-619	2.0 ± 1.5	187.5	>0.5	292	1.00E-11	2.50E-09	250	3, 3, 3, 3, 53, 53
XTE J1543-568	10	75.56	<0.03	27.12	1.00E-10	8.00E-10	8	6, 6, 6, 6, 54, 54
AX J1749.1-2733	14.5 ± 1.5	–	–	132	9.60E-12	–	–	3, –, –, 3, 7, –
GRO J1750-27	18	29.8	0.36	4.45	<2.00E-10	2.00E-09	>10	6, 6, 6, 6, 55, 55
AX J1820.5-1434	8.2 ± 3.5	54	–	152.26	1.50E-12	–	–	21, 3, –, 3, 7, –
Ginga 1843+009	10	–	–	29.5	1.06E-13	6.0E-10	5660	6, –, –, 6, 56, 57
XTE J1858+034	10[c]	380	–	221	4.80E-10	–	–	–, 3, –, 3, 6, –
4U 1901+03	10	22.58	0.04	2.76	1.00E-11	1.00E-08	1000	6, 6, 6, 6, 58, 58
KS 1947+300	9.5 ± 1.1	40.41	0.03	18.76	3.75E-12	3.00E-09	800	3, 6, 6, 6, 56, 59
EXO 2030+375	7.1 ± 0.2	46.02	0.41	42	<9.70E-12	2.70E-08	>2784	6, 6, 6, 6, 6, 6
SAX J2103.5+4545	6.5 ± 2.3	12.67	0.41	358.6	2.20E-13	1.40E-09	6364	6, 6, 6, 6, 60, 61
				Other HMXBs				
IGR J16318-4848	3.6 ± 2.6	80.09	–	–	2.30E-12	7.50E-12	3.3	7, 70&71, –, –, 7, 7
3A 2206+543	2.6	9.57	0.3	5588	1.20E-11	3.00E-09	250	3, 62, 62, 63, 6, 64

Table 2 – *continued*

Name	Dist (kpc)	P_{orb} (d)	ecc	P_{spin} (s)	F_{min} (1–10 keV) (erg cm^{-2} s^{-1})	F_{max} (1–10 keV) (erg cm^{-2} s^{-1})	$DR_{1-10\,keV}$ (F_{max}/F_{min})	References[a]
Cyg X-1	$1.86^{+0.12}_{-0.11}$	5.6	0.018	–	5.10E-09	1.90E-08	3.7	3, 3, 65, –, 7, 7
Cyg X-3	7.4 ± 1.1	0.2	0.0[d]	–	1.70E-09	8.30E-09	4.9	66, 3, –, –, 6, 6
SS 433	5.5 ± 0.2	13.08	–	–	4.00E-11	2.00E-10	5.0	6, 6, –, –, 6, 6
				Symbiotic binary				
XTE J1743-363	5	–	–	–	7.80E-12	4.80E-11	6.2	67, –, –, –, 67, 67

Notes. [a]For each source, the six numbers indicate the six references for the source distance, orbital period, eccentricity, spin period, and minimum and maximum fluxes (1–10 keV) reported in columns from 2 to 7, respectively: (1) Martínez-Núñez et al. (2017), (2) Sidoli (2017), (3) Walter et al. (2015), (4) Townsend et al. (2011), (5) Falanga et al. (2015), (6) Liu, van Paradijs & van den Heuvel (2006), (7) Giménez-García et al. (2015), (8) Sidoli, Esposito & Ducci (2010), (9) Sidoli et al. (2009), (10) Romano et al. (2009), (11) Inam, Baykal & Beklen (2010), (12) Rosen et al. (2016), (13) Saxton et al. (2008), (14) Hilditch, Howarth & Harries (2005), (15) Bodaghee et al. (2010), (16) Tomsick et al. (2009), (17) Romano et al. (2007), (18) Islam & Paul (2016), (19) Islam et al. (2015), (20) Bodaghee et al. (2016), (21) Bodaghee et al. (2012), (22) Aftab, Islam & Paul (2016), (23) Tomsick et al. (2008), (24) Coleiro & Chaty (2013), (25) Jaisawal, Naik & Paul (2013), (26) Fürst et al. (2012), (27) Torrejón et al. (2010), (28) Israel et al. (2016), (29) Sidoli et al. (2016), (30) Rodriguez et al. (2005), (31) Bozzo et al. (2017), (32) Romano (2015), (33) Sidoli et al. (2012), (34) Sidoli et al. (2013), (35) Romano et al. (2008), (36) Bozzo et al. (2012), (37) Ducci et al. (2013), (38) in't Zand (2005), (39) Romano et al. (2015), (40) Bozzo et al. (2008), (41) Boon et al. (2016), (42) Bozzo et al. (2011), (43) Reig (2011), (44) Nakajima et al. (2017), (45) Doroshenko et al. (2017), (46) Lutovinov, Tsygankov & Chernyakova (2012), (47) Ballhausen et al. (2017), (48) Kühnel et al. (2017), (49) Evans et al. (2014), (50) Cusumano et al. (2013), (51) La Palombara et al. (2009), (52) Li et al. (2012), (53) Stevens et al. (1997), (54) in't Zand, Corbet & Marshall (2001), (55) Shaw et al. (2009), (56) Tsygankov et al. (2017), (57) Piraino et al. (2000), (58) Reig & Milonaki (2016), (59) Ballhausen et al. (2016), (60) Reig et al. (2010), (61) Reig, Doroshenko & Zezas (2014), (62) Stoyanov et al. (2014), (63) Wang (2013), (64) Wang (2010), (65) Orosz et al. (2011), (66) McCollough, Corrales & Dunham (2016), (67) Bozzo et al. (2013), (68) Neilsen et al. (2009), (69) Rodes et al. (2017), (70) Jain, Paul & Dutta (2009), (71) Iyer & Paul (2017), (72) Roberts et al. (2001)

[b]The spin period of IGR J17544–2619 needs confirmation, being obtained from *RXTE*/PCA observations; it is possible that X-ray pulsations come from a different transient source within the field of view.

[c]A distance of 10 kpc for XTEJ 1858+034 is assumed.

[d]Here, we assume a circular orbit, given the short orbital period.

For each detected source j, we calculate the fluence over i, over the total number of ScWs where the source has been detected:

$$\text{Fluence}_j = \sum_{ScW_i} \text{count rate}(ScW_i) \times \text{dur}(ScW_i) \quad (1)$$

The fluence (total number of counts for each detected source j) was used to calculate an average rate, as $Rate_j = Fluence_j/\Delta t_j$, where Δt_j is the *source activity* (defined in Section 2 and reported in Table 1, third column). This average rate, $Rate_j$ was then converted into an average luminosity, L_X, in the energy range 18–50 keV (reported in Table 1, fifth column). For transient sources, this L_X is the average luminosity observed by *INTEGRAL* when the source is in outburst. In Table 1, we show also the minimum and maximum 18–50 keV luminosities displayed by each source (always at ScW level, bin time of ∼2 ks), as observed by *INTEGRAL* (cols. 6 and 7), together with their ratio (col. 9), that represent the maximum source variability observed by *INTEGRAL* in 14 years. We note that for a highly variable source, the average hard X-ray luminosity might be, in principle, more affected by the source distance than the maximum luminosity. However, the average value is more representative of the source global behavior, while the maximum luminosity, being derived from a single 2 ks *INTEGRAL* observation, might be reached during a rare short flare, brighter than the usual source intensity.

No statistical error is given on the average rate (or L_X), because the largest source of uncertainty in the hard X–ray luminosities is due to the source distance, reported in Table 2. When the uncertainty is not listed, it is because we could not find it in the literature. For these sources, we have assumed ±1 kpc. However, the uncertainty on the source luminosities has no impact on our conclusions.

3.2 Cumulative luminosity distributions (18–50 keV)

The long-term IBIS/ISGRI light curves (∼2 ks bin time) were used to build the *complementary cumulative luminosity distribution functions* (hereafter, only cumulative luminosity distributions, CLDs) of the hard X–ray emission for our sample of HMXBs. In Paizis & Sidoli (2014), we investigated the CLDs of the SFXT flares caught by *INTEGRAL* in nine years of observations, and compared them to three classical HMXBs. Here, we enlarge our investigation on a larger data set (14 years) to different types of massive X–ray binaries, to compare their behaviour in terms of source activity and variability amplitude in hard X–rays.

In Figs 1, 2, 3, and 4, we show the normalized CLDs for different sub-classes of HMXBs: SFXTs, SgHMXBs, Be/XRBs, and 'other sources' including BH binaries. The normalization of each curve has been performed with respect to the total exposure time for which the source was within 12°. In this way, the source $DC_{18-50\,keV}$ (per centage of time in which the source is active at ScW level) can be derived directly from the CLD as the highest value in the y-axis (and it is also reported in Table 1). Not only can the variability amplitude of the source luminosity (shown in 14 years of *INTEGRAL* mission) be read from the x-axis in each source CLD, but also the per centage of time spent by each source in different luminosity states can be derived.

Transient versus persistent behaviour depends both on the intrinsic variability and on the instrumental sensitivity threshold. In principle also, the source distance might contribute (but see Fig. 11 and Section 5.2.1). As can be seen from the CLDs (and from the Table 1), only the Crab and Cyg X-1 are always detected. Persistent, eclipsing HMXBs (marked in Table 1 with an asterisk), show a lower $DC_{18-50\,keV}$ because *INTEGRAL* is not able to detect the sources in eclipse on time-scales of a single ScW. The less active (more transient) the source, the lower the $DC_{18-50\,keV}$. Furthermore, the more variable the hard X–ray luminosity (at ∼2 ks timescale), the flatter the CLD. A persistent, bright, and constant source seen by an ideal detector would display a CLD as a vertical straight line. In real life, the Crab shows a deviation (Figs 1, 2, 3, and 4) that includes both the intrinsic intensity decline, observed in the Crab by

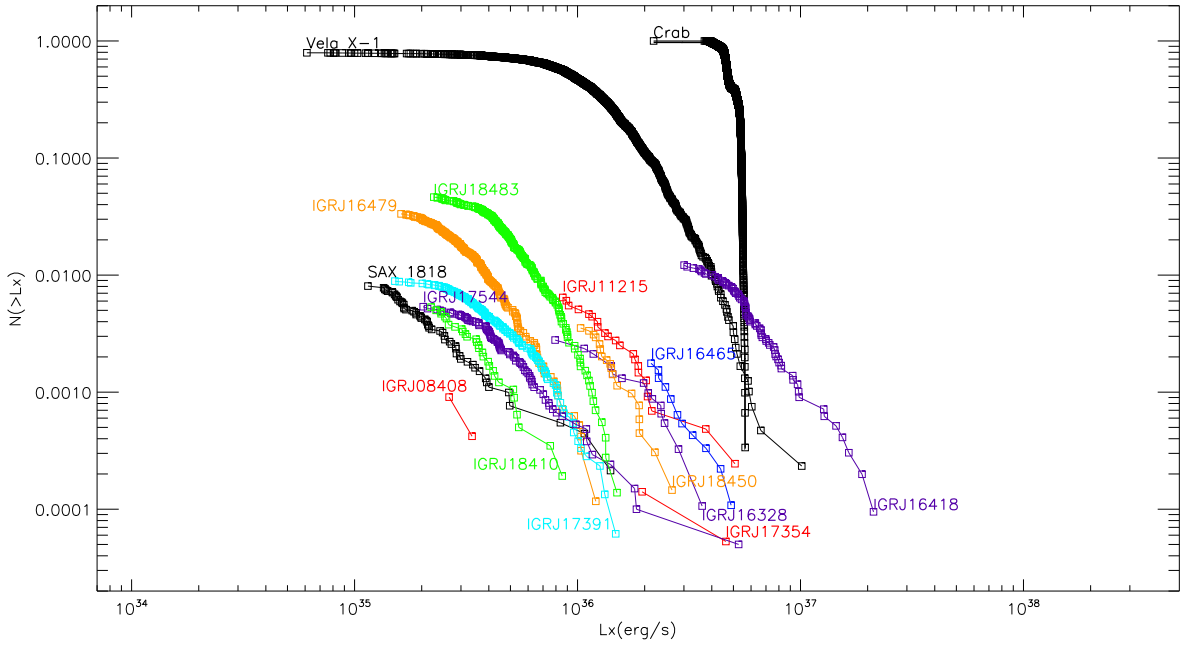

Figure 1. Cumulative luminosity (18–50 keV) distributions of SFXT flares. Each data point is a ScW based detection (detection significance ≥5). Vela X–1 and the Crab are shown for comparison.

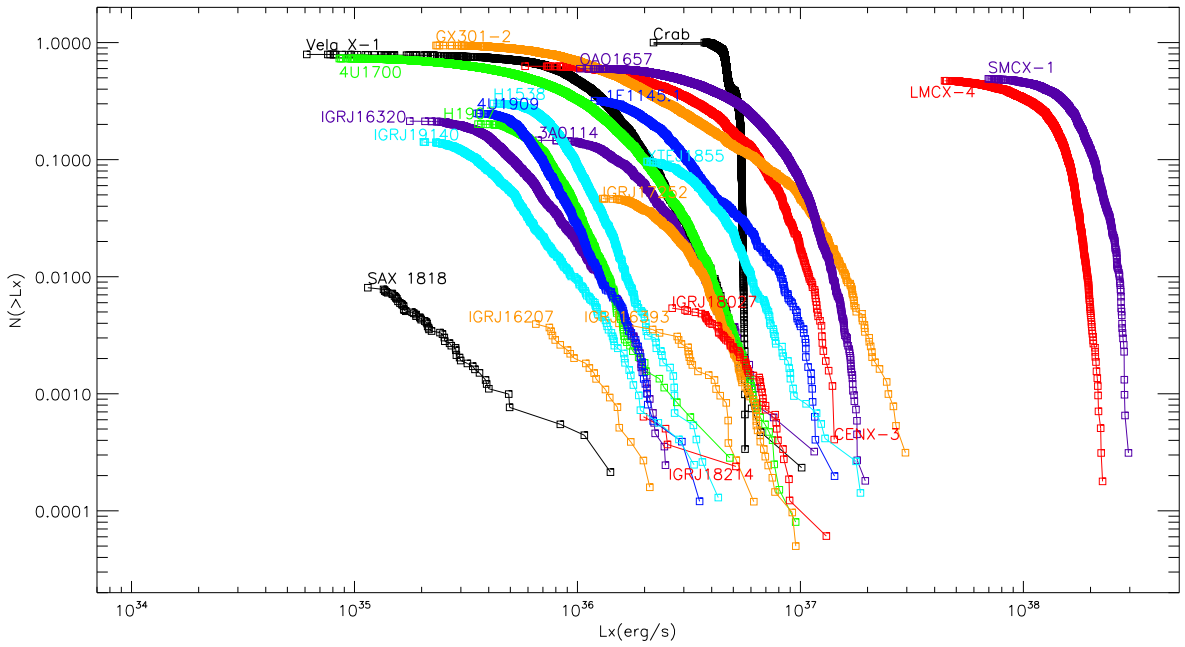

Figure 2. Cumulative luminosity (18–50 keV) distributions of SgHMXBs, compared with one SFXT (SAX J1818.6-1703) and the Crab.

several instruments (Wilson-Hodge et al. 2011), and the IBIS/ISGRI loss of sensitivity. These two effects cannot be disentangled in the CLDs. However the Crab CLD indicates the amount of variability beyond which a source can be safely considered as intrinsically variable.

4 HMXBS PROPERTIES COLLECTED FROM THE LITERATURE

For each HMXB in our sample, we searched through the literature to collect available information about the source distance, spin and orbital periodicities, orbital eccentricity, minimum and maximum flux in soft X–rays (1–10 keV, corrected for the absorption). We list these quantities in Table 2. We relied on a number of review papers. This implies that the references reported in Table 2 (last column) for a particular parameter is not, in most cases, the original discovery paper, but a more recent review article collecting previous literature about a large number of sources. This has also the advantage that up-to-date values for these quantities are reported in Table 2.

We caution that the minimum and maximum unabsorbed fluxes (1–10 keV) taken from the literature have been obtained with different instruments and are integrated over different time-scales. For

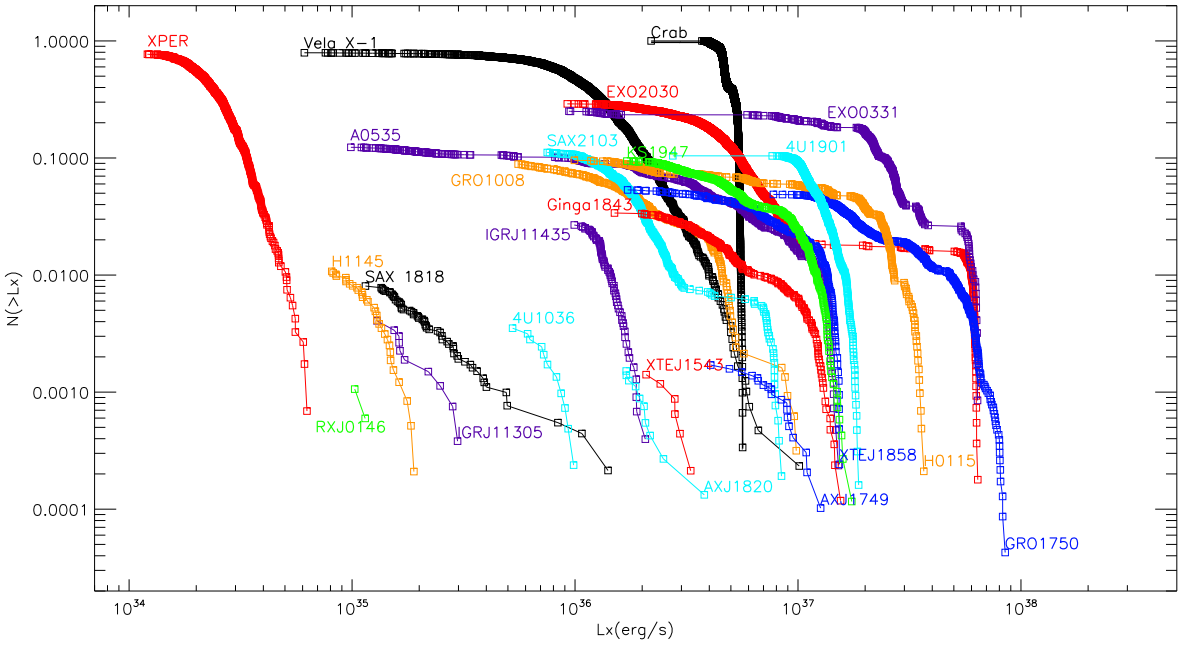

Figure 3. Cumulative luminosity (18–50 keV) distributions of Be/XRBs, compared with one SFXT (SAX J1818.6-1703), one persistent SgHMXB (Vela X–1) and the Crab.

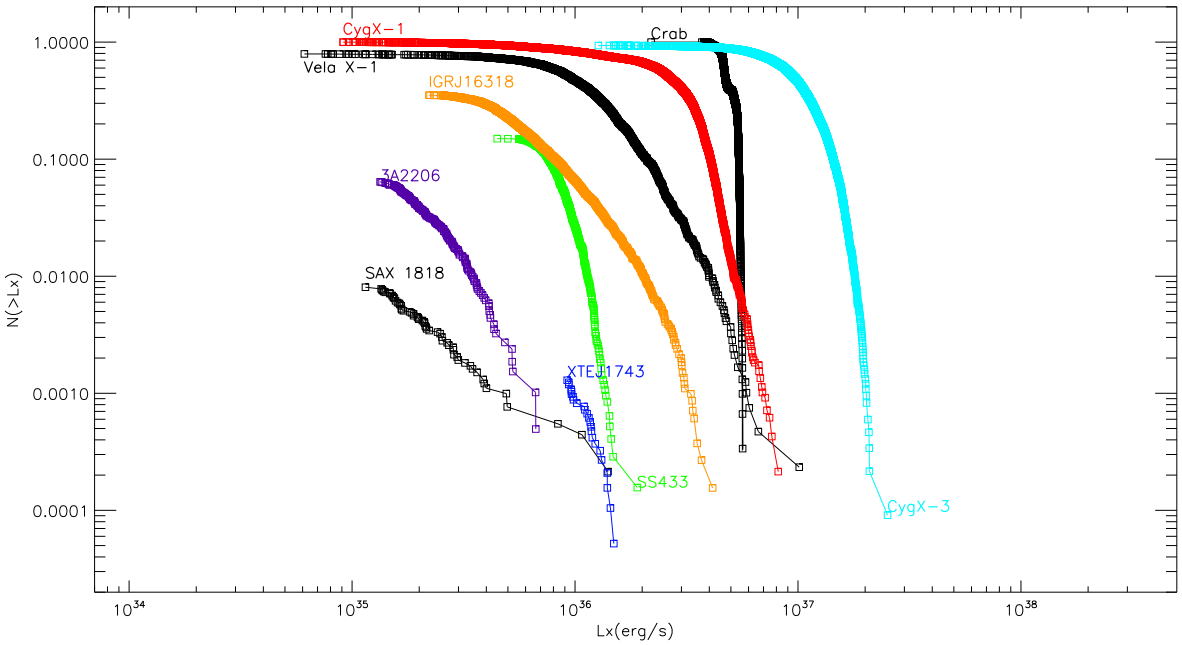

Figure 4. Cumulative luminosity (18–50 keV) distributions of BH and peculiar sources, compared with one SFXT (SAX J1818.6-1703), one persistent SgHMXB (Vela X–1) and the Crab.

instance, some of the soft X-ray fluxes have been derived from dedicated monitoring campaigns (as in the case of a sample of SFXTs monitored by Swift/XRT, Romano (2015)), while others have been taken from papers reporting on deep exposures performed with high-throughput instruments, like EPIC on-board *XMM-Newton* (Giménez-García et al. 2015). Moreover, an obvious bias arises when collecting values from the literature, as only a new result is usually reported in a paper. It is possible that rarer intensity states (implying a larger dynamic range than the one listed in Table 2) await discovery.

Normally, fluxes integrated over different soft energy ranges are reported in the literature. Hence, for consistency's sake, we extrapolated them to the 1–10 keV band, using WEBPIMMS[2] and the appropriate spectral model reported in the same paper. If more complex best-fit models than the ones present in WEBPIMMS are reported in the literature, we used XSPEC (Arnaud 1996) to extrapolate the soft X-ray fluxes. We never extrapolated hard X-ray fluxes

[2]https://heasarc.gsfc.nasa.gov/cgi-bin/Tools/w3pimms/w3pimms.pl

(E>20 keV) to the 1–10 keV energy band, since these values would be largely unreliable, given the presence of a high-nergy cutoff in HMXB pulsars spectra, around 10–30 keV.

For X-ray pulsars, we only considered spin-phase-averaged fluxes. Since we are interested in the intrinsic flux variability, we report here out-of-eclipse values, for well-known eclipsing HMXBs. Sometimes this information is not clearly reported in the literature, especially when dealing with X-ray catalogues. In this respect, the review paper of Fe line properties by Giménez-García et al. (2015) is notable, in clearly flagging the *XMM-Newton* observations performed during X-ray eclipses in their large sample of HMXBs.

From the maximum and minimum 1–10 keV fluxes, we then calculated their ratio, i.e. the dynamic range '$DR_{1-10\,keV}$' (see Table 2, col. 8). This variability amplitude is indeed one of the properties used to define SFXTs (see Sidoli 2017 for the most recent review) compared with other, more steady, SgHMXBs. If only a single measurement of the soft X–ray flux has been found in the literature, we assigned it to the minimum 1–10 keV flux. In this case, we did not calculate the $DR_{1-10\,keV}$.

5 DISCUSSION

We discuss here the hard X–ray results obtained from the *INTEGRAL* archive spanning 14 years (Section 5.1 and Table 1) and put these results into context of soft X-ray dynamic ranges and other interesting source properties (Section 5.2 and Table 2).

5.1 Characterizing the cumulative hard X–ray luminosity distributions

For all the sources of our sample we extracted the CLDs, expanding our previous investigation of the CDLs of a number of SFXTs with *INTEGRAL* (Paizis & Sidoli 2014). They are reported in Figs 1, 2, 3, and 4, for the different sub-classes of HMXBs.

5.1.1 General remarks on CLDs

Before discussing the single CLDs, it is important to remark that there are two features in the CLDs that need to be taken into account: a turn-over is often present at both low and high luminosities. The low luminosity one is due to the difficulty to detect faint X–ray emission, near the sensitivity threshold of the detector. This means that the sampling is not complete approaching the faintest luminosity level of each source, but it is only above a so-called *truncation point* (see Paizis & Sidoli 2014 for more details). A high-luminosity cutoff can be observed as well in some CLDs, because of either a real presence of a maximum X-ray luminosity or because of the fact that the long-term *INTEGRAL* monitoring is still not long enough to observe the most luminous, rare, X–ray flaring activity. This implies a large uncertainty in the high-luminosity part of the CDL of the most variable and transient sources (SFXTs). These two effects combined imply that the most robust part of a CLD is in-between these two cutoff luminosities, especially for SFXTs.

In Figs 1, 2, 3, and 4, the CLDs for different types of HMXBs are displayed. Note that we always display, as reference on each plot, the CLDs of the Crab, of Vela X–1 (prototype of persistent SgHMXBs) and of the prototypical SFXT SAX J1818.6–1703. These plots report remarkably different CLD shapes depending on the source sub-class.

We plot in Figs 5 and 6, as an example, the differential luminosity distributions of four sources, to show how the features characterizing the CLDs are related with the histograms of the source luminosity, detected at ScW level, and to their long-term light curves. In particular, when a peak is present in the histogram, the correspondent CLD shows a curved feature (a more or less pronounced knee). The narrower the peak in the histogram, the steeper the knee in the CLD. A multimodal histogram translates into multiple knees in the CLD (as the one shown by Be/XRTs, that we will discuss below). From this comparison it is also clear about the advantage of using the cumulative, instead of differential, distributions: in the cumulative distribution, there is no need to arbitrarily bin the data, so that all information is retained. This is especially crucial when the number of the detections is not very large (SFXTs). Moreover, from the normalized CLDs, it is immediately possible to visualize the source $DC_{18-50\,keV}$, the luminosity range of variability, the median luminosity. Since we focus here on global (integrated over time) characteristics of HMXB sub-classes, we will not discuss the source X–ray light curves further.

5.1.2 SFXT CLDs

In Fig. 1, we show the CLD of the SFXTs, where it is evident about the very low (a few per cent) $DC_{18-50\,keV}$ of the flaring activity from these transients. We remark that the SFXT CLDs reported here can be considered as the CLDs of the SFXT flares, given the similar time-scale of both the ScWs and X–ray flare duration. We have already discussed this point in Paizis & Sidoli (2014), to which we refer the reader. In Paizis & Sidoli (2014), we compared the CLDs of the SFXT flares extracted from about nine years of *INTEGRAL* data, with the CLD shown by three classical HMXB systems: two persistent (Vela X–1 and 4U 1700–377) and one (likely transient) SgHMXB with highly variable X-ray emission (H 1907 + 09). The CLDs of the SFXT X-ray flares were found to be well represented by power-law models, while log-normal-like functions were a more plausible representation of the CLD of the other three classical SgHMXBs. The SFXT CLDs are confirmed to be well described by power-law models also in the larger data-base we are reporting here (14 years of *INTEGRAL* mission instead of 9), showing slopes consistent with the ones reported in our previous investigation (Paizis & Sidoli 2014). Indeed, following the same procedure as in Paizis & Sidoli (2014), we characterized the CLDs of SFXT flares adopting a power-law model. In Table 3, we report the results, quoting the luminosity of the truncation point adopted for each SFXT flare luminosity distribution, the resulting power-law slope and the corresponding Kolmogorov–Smirnov (KS) probability. The power-law slopes are consistent, within their uncertainties, with previous values reported by Paizis & Sidoli (2014) analysing nine years of *INTEGRAL* data. Only in case of IGR J16418–4532 is the power-law steeper (slope of 2.28 ± 0.40, compared to previous value of 1.31 ± 0.31). The steeper slope of the CLD is produced by the most recent flares detected from this source (later than April 2012). These flares are not included in Paizis & Sidoli (2014) - who considered data up to April 2012 – and lie in a narrow range of intermediate luminosities, from 5×10^{36} erg s^{-1} to about 8×10^{36} erg s^{-1}, resulting in a different overall slope of the distribution. Moreover, we can now add to our sample two more SFXT sources, given the larger *INTEGRAL* database (IGR J16328–4726 and IGR J16465–4507).

SFXTs show similar, very small $DC_{18-50\,keV}$ (<5 per cent). As previously observed, the SFXTs with the highest $DC_{18-50\,keV}$, in the range from 1 to 5 per cent, are confirmed to be the so-called

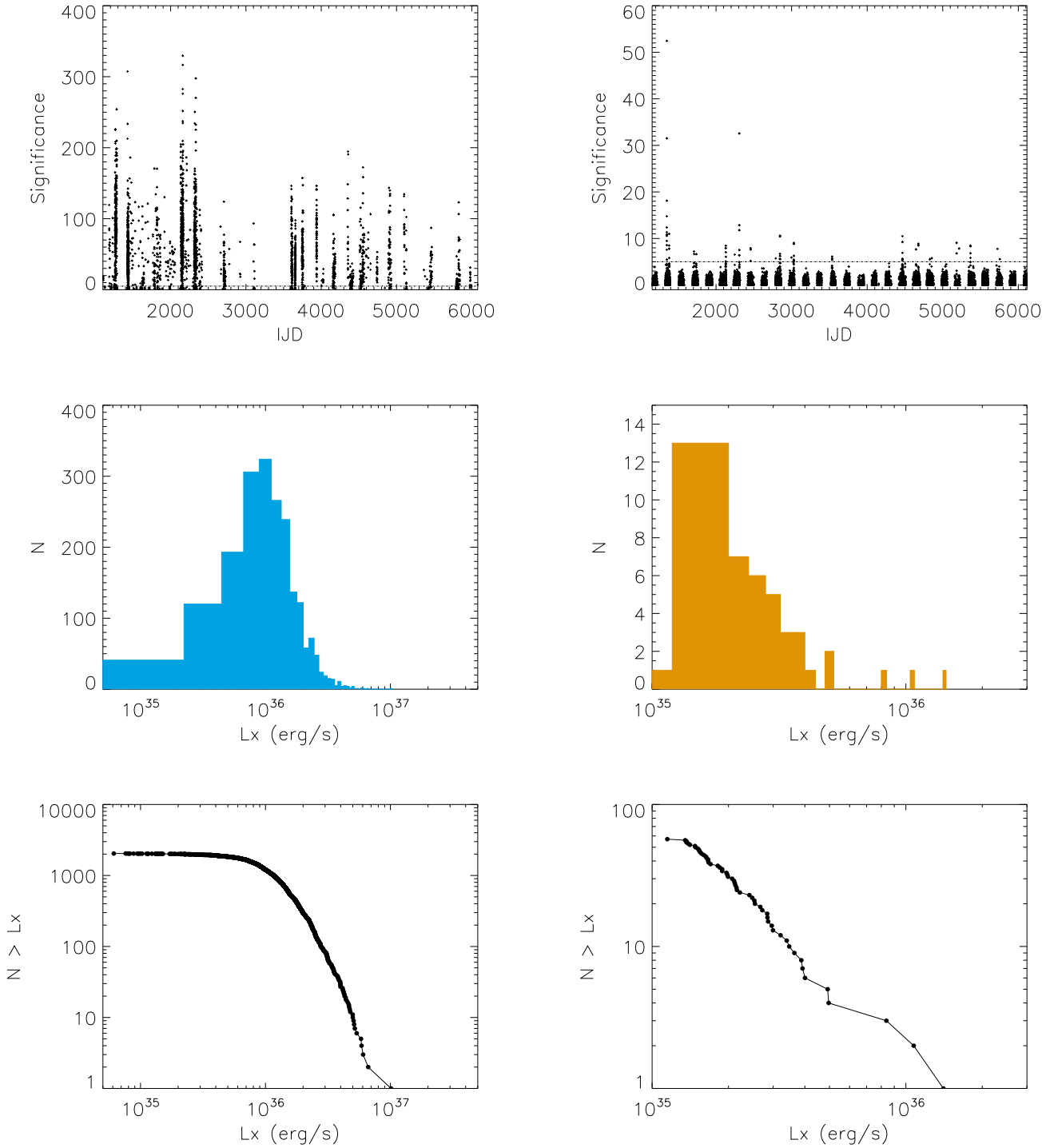

Figure 5. *Left-hand panels:* Vela X–1 behaviour in the *INTEGRAL* archive, as representative of SgHMXBs. From top to bottom: source light curve (detection significance in the energy range 18–50 keV, versus time in units of *INTEGRAL* JD − IJD = MJD-51544, together with a 5σ horizontal line), histogram of the detection occurrence and, last panel, its non-normalized CLD. *Right-hand panels:* the same for SAX J1818.6–1703, as an example of SFXTs.

'intermediate SFXTs' (IGR J16418–4532, IGR J16479–4514 and IGR J18483–0311), which are more active than other, prototypical, SFXTs. In this work two more SFXTs are included in our sample: IGR J16328–4726 and IGR J17354–3255, that resulted in very low $DC_{18-50\,keV}$, as well (0.28 and 0.01 per cent, respectively).

5.1.3 *SgHMXB CLDs*

SgHMXB CLDs are shown in Fig. 2, together with two sources hosting an early-type giant companion, LMC X-4 and Cen X–3. Most of these CLDs show a completely different behaviour with respect to SFXTs, not only in their high $DC_{18-50\,keV}$ (indeed, many

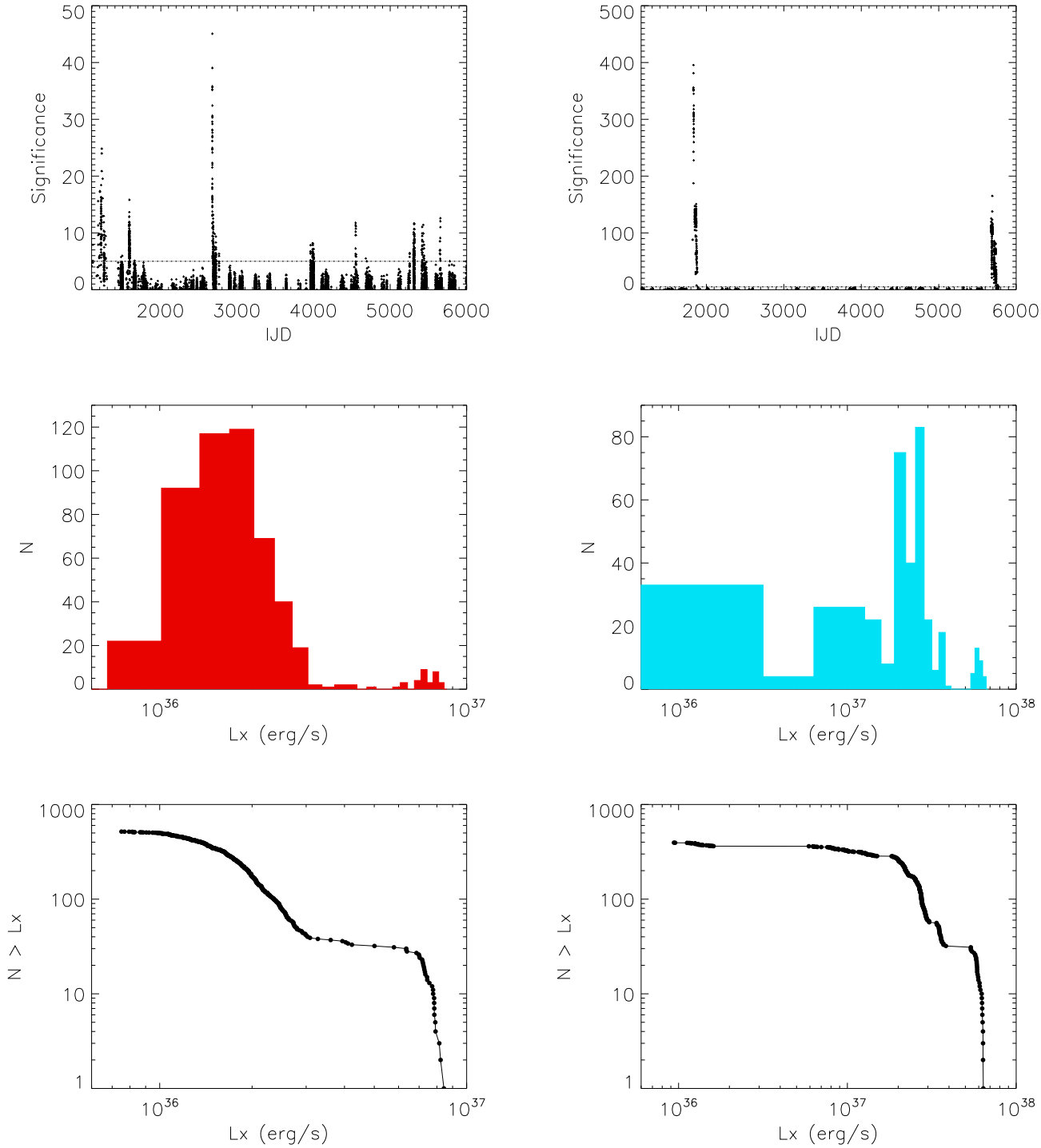

Figure 6. Same as Fig. 5 for two Be/XRTs: SAX J2103.5+4545 (on the left) and EXO 0331+530 (on the right).

SgHMXB are classified in the literature as persistent X–ray sources) but also in the shape of their CLD, that appears closer to a log-normal function (e.g. Vela X–1; see also Fig. 5, left-hand panels). We did not attempt to perform an analytical description of these CLDs, which display many different shapes. Indeed, in these brightest sources, many effects, like orbital and super-orbital modulations of the X-ray light curves, as well as aperiodic trends, can modify the shape of the CLDs.

Globally, the CLDs of classical HMXBs hosting giant or supergiant donors appear unimodal and can be more (like in SMC X–1 and LMC X–4) or less (like in OAO 1657–415, Cen X–3) peaked. The highest luminosities are reached by SMC X–1 and LMC X–4, that are Roche lobe overflow (RLO) systems, allowing the formation of an accretion disc, sustaining a much higher mass transfer rate onto the pulsar than in wind-fed systems. Excluding these two systems, the HMXBs shown in Fig. 2 reaching the high-

Table 3. Maximum likelihood estimation of the power-law parameters of the CLD (18–50 keV) of SFXT flares.

Name	Truncation point L_X (10^{35} erg s^{-1})	Power-law slope	KS prob.
XTE J1739–302	6.3	2.85 ± 0.73	0.999
IGR J17544–2619	4.1	2.12 ± 0.32	0.947
SAX J1818.6–1703	1.5	1.76 ± 0.29	0.993
IGR J16418–4532	50.0	2.28 ± 0.40	0.934
IGR J16479–4514	3.4	2.56 ± 0.32	0.999
IGR J18483–0311	4.1	2.24 ± 0.23	0.999
IGR J18483–0311	9.7	3.25 ± 1.14	0.999
IGR J18450–0435	11.2	2.12 ± 0.76	0.989
IGR J18410–0535	3.6	2.65 ± 1.04	0.985
IGR J11215–5952	11.0	1.76 ± 0.60	0.805
IGRJ 16328–4726	20.0	3.2 ± 1.7	0.968
IGR J16465–4507	21.0	1.5 ± 0.6	0.996

est luminosity are GX 301–2, OAO 1657-415 and Cen X–3. These findings are in agreement with what is known about these sources. GX 301–2 is the only system with a B-type hypergiant donor (Wray 977) that displays a huge mass loss rate ($\dot{M}_w = 10^{-5}\ M_\odot$ yr^{-1}; Kaper, van der Meer & Najarro 2006) and a slow wind (terminal velocity, v_∞, ∼300 km s^{-1}), explaining the high X-ray luminosity compared to other wind accretors. Cen X–3 is an eclipsing, persistent HMXBs, where RLO is thought to take place, and the accretion occurs through a disc (Bonnet-Bidaud & van der Klis 1979). OAO 1657-415 is an eclipsing HMXBs that is located between the Be and SgHMXB systems on the Corbet diagram (spin versus orbital period), suggested to alternate wind acretion with disc accretion phases, sustaining a higher X–ray luminosity (Audley et al. 2006). It is interesting to note that the shape of the CLDs in OAO 1657-415 and Cen X–3 appears very similar, probably because of the presence of an accretion disc most of the time in OAO 1657-415 too.

The eclipsing HMXBs show a lower $DC_{18-50\,keV}$, reduced by the non-detection with IBIS/ISGRI during X–ray eclipses. Also short, intrinsic drops of flux (the so-called off-states), might led to a lower $DC_{18-50\,keV}$ at 2 ks time bin (Kreykenbohm et al. 2008; Sidoli et al. 2015). In other sources, the low $DC_{18-50\,keV}$ is to be ascribed only to an intrinsic X–ray intensity variability. This is the case of IGR J19140+0951, where the large variability of its X–ray flux is confirmed at softer energies (Sidoli et al. 2016). The presence of the SgHMXB H1907+097 in this group, known to be in-between persistent and transient sources (Doroshenko et al. 2012), strengthens the interpretation of these sources as truly highly variable SgHMXBs.

There is also a group of SgHMXBs in Fig. 2 which displays a very low $DC_{18-50\,keV}$ (below 1 per cent, IGR J16207-5129, IGR J16393-4643, IGR J18027-2016 and IGR J18214-1318), similar to SFXTs, indicative of either transient emission, or persistent but faint emission, just below the threshold of detectability of IBIS/ISGRI, that might be detected only during some flaring activity. This phenomenology might suggest that within HMXBs with supergiant companions there is a smooth transition from persistent sources to SFXTs.

From the visual inspection of Fig. 2, it is tempting to see an evolution in the shape of the CLDs, from steeper (at high $DC_{18-50\,keV}$ and high median luminosity) to flatter ones (at lower $DC_{18-50\,keV}$ and lower luminosity). In particular, there seems to be a transition from LMC X–4 and SMC X–1 CLDs, which share a very similar shape (high $DC_{18-50\,keV}$, more peaked, less variable and with a higher median luminosity) through Cen X–3 and OAO 1657–415 (less peaked CLDs, at lower luminosity) down to IGR J16320–4751 and IGR J19140+0951 (with a much flatter CLD, lower luminosity and lower $DC_{18-50\,keV}$, almost announcing the power-law-like CLDs of the SFXT flares). To investigate this apparent trend in a more quantitative way, we calculated the skewness of the SgHMXB luminosity distributions, defined as follows:

$$\mathrm{Skewness}_j = \frac{1}{N}\sum_{i=0}^{N-1}\left(\frac{x_i - \bar{x}}{\sqrt{\mathrm{Variance}_j}}\right)^3 \quad (2)$$

where, for each source j, N is the total number of detections, x_i is the source luminosity during the ith observation, and $\bar{x}$ is the mean luminosity. We selected the best defined and populated distributions, with a $DC_{18-50\,keV}$ larger than 1 per cent, and we explored their dependence on the median luminosity (Fig. 7, left-hand panel). We found an anticorrelation, confirmed by the adoption of the Spearman's correlation coefficient, r_s ($r_s = -0.685$, $n = 16$, p-value = 0.00339). Other relations between the skewness of the luminosity distributions and the source parameters were investigated, finding a significant correlation with the pulsar spin period (Fig. 7, right-hand panel), confirmed by running the Spearman's correlation ($r_s = 0.693$, $n = 15$, p-value = 0.0042). The source 4U1700-37 was excluded, since the pulsation is not known. This dependence extends over several orders of magnitude and might be partly explained by the known anticorrelation between the (maximum) X–ray luminosity and the rotational period (Stella, White & Rosner 1986; in faster pulsars, the centrifugal barrier enables accretion only at higher accretion rates). However, the new finding here is that, not only does the spin anticorrelate with the median of the X-ray luminosity in SgHMXBs, but also the shape of the luminosity distribution is important: the fastest SgHMXB pulsars are found not only in the most luminous sources, but also where the X-ray luminosity distribution is more symmetric and peaked. This is the case of RLO-systems, where an accretion disc forms around the neutron star (LMC X–4, SMC X–1, Cen X–3). More and more skewed CLDs are present in more variable (or transient) wind-fed accretors, hampering an effective pulsar spin-up. Also longer orbital periods and more eccentric orbits play a role, resulting in a stronger correlation of the CLD's skewness with the binary eccentricity [$r_s = 0.606$, $n = 14$, $p = 0.0217$] than with the orbital period [$r_s = 0.376$, $n = 16$, $p = 0.151$]. This implies that the periodic modulation of the X–ray emission expected in wind-fed eccentric SgHMXBs produces a significantly skewed CLD.

5.1.4 *Be/XRB CLDs*

Transient Be/XRBs show significantly different CLDs (Fig. 3), in many respects. Many Be systems have $DC_{18-50\,keV}$ around ∼10 per cent and show bi- or multi-modal CLDs: wave-like structures in the CLDs correspond to peaks in the histograms (see Fig. 6), indicative of different populations of outbursts, or multi-peaked outbursts, and/or transitions to different regimes. In the CLD of two transients, EXO 2030+375 and SAX J2103.5+4545, an almost horizontal plateaux (more or less populated by detections) is located at intermediate luminosities, a bridge between two different kind of outbursts, the faintest (and more frequent) ones and the most luminous (and less frequent), ones. This step-like CLDs shape is the signature of Be/XRTs showing both Type I and Type II outbursts.

Be/XRTs are known to display two kinds of outbursts (Stella et al. 1986; Negueruela et al. 1998, see also Reig 2011 and Kuehnel et al. 2015 for reviews). Type I (also named 'normal') outbursts are periodic and triggered near the periastron passage, by an enhanced

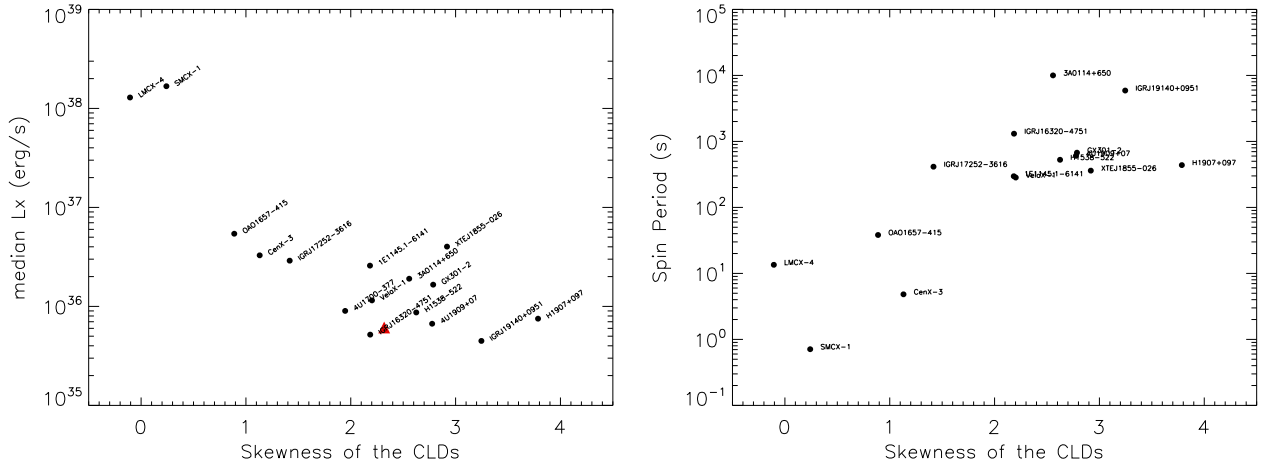

Figure 7. Median luminosity (18–50 keV; left-hand panel) and pulsar spin period (right-hand panel) versus the skewness of the CLDs, for giant and supergiant HMXBs with $DC_{18-50\,keV}$ larger than 1 per cent. The red triangle on the left-hand panel indicates the position of the SgB[e] binary IGR J16318–4848 (see Section 5.1.5).

accretion rate onto the neutron star (NS) by material captured from the circumstellar decretion disc, expelled by the Be companion (Negueruela & Okazaki 2001; Negueruela et al. 2001; Okazaki & Negueruela 2001). Their durations are usually a fraction (0.2–0.3) of the orbital period. The physical mechanism driving the formation of the Be disc is still unclear, although it might be due to both rapid rotation and nonradial pulsations (Baade et al. 2017). Type II (also named 'giant') outbursts can be observed at any orbital phase and are more luminous (and rarer) than Type I outbursts, sometimes reaching the Eddington luminosity. They can show a duration much larger than one orbital cycle and are thought to be caused by major changes in the structure of the Be decretion disc, likely linked to some warping episodes (Okazaki, Hayasaki & Moritani 2013), although the details of the accretion mechanism remain elusive. In any case, there is observational evidence that the Be circumstellar disc undergoes a quasi-cyclic build-up and desruption (Negueruela et al. 2001). Also intermediate-luminosity outbursts have been observed (Caballero-García et al. 2016), making the situation more complicated.

Different spectral states have been recognized in Be/XRTs during giant outbursts (Reig 2008; Reig & Nespoli 2013), from two different patterns observed in the hardness-intensity diagrams: a horizontal branch, which corresponds to a low-intensity state, and a diagonal branch, emerging only when the X–ray luminosity exceeds a critical limit, L_{crit}. This critical value depends on the NS magnetic field strength as $L_{crit} \sim 1.28 \times 10^{37}\,(E_{cyc}/10\,keV)^{16/15}$ erg s^{-1}, where E_{cyc} is the centroid energy of the cyclotron resonance scattering feature (CRSF; Becker et al. 2012). Two different accretion regimes, above and below L_{crit} (that represents a threshold for the formation of a radiative-dominated shock that decelerates the accretion flow above the NS surface), also explain the bimodal variation (correlation or anti-corrrelation) of the energy of the CRSF with the X–ray luminosity (Becker et al. 2012). In Table 4 (col. 4) we list the critical luminosities for sources (a few Be/XRBs, SgHMXBs, and one SFXT) where cyclotron lines have been discovered. Sometimes, spin-up episodes during Be/XRBs outbursts have been observed, indicating the formation of an accretion disc around the NS (Baykal, Stark & Swank 2002).

In the CLD of the Be transient EXO 0331+53, two empty horizontal plateaux are present, characterized by luminosity jumps.

Table 4. Expected lowest X–ray luminosity $L_{propeller}$, at the onset of the propeller effect (see equation 3), together with the critical luminosity, L_{crit}. B is the NS magnetic field in units of 10^{12} G, z is the NS gravitational redshift (values taken from Revnivtsev & Mereghetti 2015).

Source	$B/(1+z)$ (10^{12} G)	$L_{propeller}$ (erg s^{-1})	L_{crit} (erg s^{-1})
Vela X-1	2.1	3.3×10^{32}	3.4×10^{37}
GX 301-2	3.0	8.8×10^{31}	4.9×10^{37}
H 1538-522	2.0	7.0×10^{31}	3.1×10^{37}
H 1907+097	1.5	6.0×10^{31}	2.4×10^{37}
Cen X-3	2.6	6.7×10^{36}	4.1×10^{37}
IGRJ17544-2619	1.5	4.1×10^{33}	2.3×10^{37}
H 0115+634	1.0	2.0×10^{36}	1.4×10^{37}
EXO 0331+530	2.2	6.0×10^{36}	3.5×10^{37}
X Per	2.5	3.7×10^{31}	4.0×10^{37}
1A 0535+262	4.0	1.2×10^{34}	6.5×10^{37}
GRO J1008-57	6.7	4.4×10^{34}	1.1×10^{38}
KS 1947+300	1.0	4.2×10^{34}	1.6×10^{37}

Since we are dealing with cumulative luminosity distributions that are integrated quantities where the temporal behaviour is lost, we cannot say if the non-detections are real or if it is because there are no *INTEGRAL* observations covering these luminosity states. The luminosity jumps might indicate the transition to a different regime, possibly the on-set of a propeller state (e.g. a centrifugal inhibition of the accretion, Campana et al. 2017). The limiting X–ray luminosity for the onset of the propeller depends on the pulsar spin period and its magnetic field, as follows (Campana et al. 2002):

$$L_{propeller} \simeq 3.9 \times 10^{37} \xi^{7/2} B_{12}^2 P_{spin}^{-7/3} M_{1.4}^{-2/3} R_6^5 \ ergs^{-1} \quad (3)$$

where the NS magnetic field, B_{12}, is in units of 10^{12} G, the pulsar spin period, P_{spin}, is in seconds; $M_{1.4}$ and R_6 are the NS mass and radius, in units of $1.4\,M_\odot$ and 10^6 cm. We here assume $\xi = 1$, appropriate for spherical accretion (note that $\xi = 0.5$ is for disc accretion).

Assuming the NS magnetic field strength reported by Revnivtsev & Mereghetti (2015) (their table 1, as estimated from the CRSF centroid energy), and the pulsar spin periods, we obtain the lowest X–ray luminosity listed in Table 4. However, $L_{propeller}$ is a bolometric

luminosity. Although we have never attempted to extrapolate hard X-ray luminosities to a broader (bolometric) energy range, we can obtain a rough idea of the conversion factor from the energy range 18–50 keV to a wider band (0.1–100 keV), re-analysing the *XMM-Newton* plus *NuSTAR* simultaneous spectrum of an accreting pulsar during an outburst, the SFXT IGR J11215–5952 (Sidoli et al. 2017). We found that $L_{0.1-100\,\mathrm{keV}} \sim 3 \times L_{18-50\,\mathrm{keV}}$. Comparing (one third of) the values reported in Table 4 with the CLDs, we find that only in two sources is there a possible overlap with $L_{\mathrm{propeller}}$: Cen X-3 and EXO 0331+530. While in the persistent pulsar Cen X–3, there is no evidence for luminosity jumps in the CLD (possibly indicative of a more appropriate ξ value of 0.5 in equation 3), the low luminosity gap observed in the transient EXO 0331+530 is in agreement with the onset of a propeller state. However, from the inspection of its hard X–ray light curve, we found that this low-luminosity gap is actually due to a missing *INTEGRAL* coverage of the declining part of the second outburst, visible in Fig. 6 (top right-hand panel).

Adopting the same conversion factor (of 3) between hard X–ray luminosities and critical luminosities calculated in Table 4, we conclude that all sources reported in this table experienced sub-critical regimes, except four systems, where L_{crit} might fall in-between the variability range of their X–ray luminosity: GX 301-2 and the three Be/XRTs H 0115+634, EXO 0331+530, and KS 1947+300.

In other Be/XRBs, there are a number of different behaviours: in some sources the bi-modality in the CLD is present, but with no plateaux in clearly separating two population of outbursts (*Ginga* 1843+009). The same is true for the multi-modality in the CLDs apparent in other Be transients (GRO J1750–27, H 0115+634, 1A 0535+262, 4U 1901+03, XTE J1858+034), where outbursts reaching different peak luminosity have been caught by *INTEGRAL* or where multi-peaked giant outbursts were observed. In this respect, the *INTEGRAL* archival observations suggest a more complex behaviour of Be/XRT outbursts, than a simple distinction in 'normal' and 'giant' outbursts.

Another remarkable feature in the Be/XRT CLDs is the sharp, almost vertical, maximum luminosity, indicative of a constant, flat-topped, giant outburst peak (GRO J1750–27, EXO 0331+530, EXO 2030+375, H 0115+634, 4U 1901+03, SAX J2103.5+4545, KS 1947+300).

In Fig 3, there are also Be sources located in the lower luminosity range of the plot. A distinctive behaviour is shown by X Per, which is almost always detected by *INTEGRAL* and displays a low luminosity with a median value of 2.4×10^{34} erg s^{-1}. X Per is the prototype of a small sub-class of Be XRBs showing persistent and low luminosity ($\sim 10^{34}$ erg s^{-1}), with long spin periods and wide, low eccentricity, orbits (Reig & Roche 1999; Pfahl et al. 2002). Other Be/XRBs belonging to this group are RX J0146.9+6121, 4U 1036-56 (aka RX J1037.5-564), RX J0440.9+4431 (La Palombara et al. 2009; Reig 2011), with the first two sources also belonging to our sample. However, as observed by *INTEGRAL*, RX J0146.9+6121 and 4U 1036-56 appear as transients, with a very low duty cycle (0.11 and 0.35 per cent, respectively), likely the high-luminosity tail of a flaring variable X–ray emission.

5.1.5 *Other sources: BH and peculiar source CLDs*

In Fig. 4, the CLDs of other massive binaries, black hole binaries (BHB) together with some peculiar sources not included in the three main sub-classes, are shown. The highest $\mathrm{DC}_{18-50\,\mathrm{keV}}$ and the largest variability is shown by the persistent BHB Cyg X-1. It is characterized by a bimodal distribution of its hard X–ray luminosity

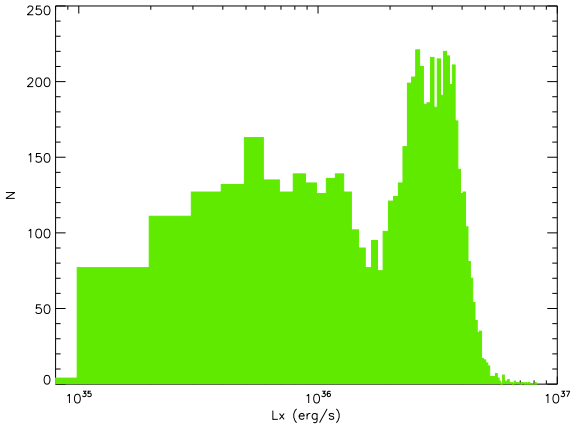

Figure 8. Cyg X–1 luminosity distribution (18–50 keV). Here, the bimodality is more evident than in the correspondent CLD shown in Fig. 4.

distribution, more clearly evident in the histogram of the luminosity detections reported in Fig. 8. In fact, this bimodality is not very clear from its normalized cumulative distribution, since the logarithmic scale compresses the curve, close to one. A more frequent source state peaks at 3×10^{36} erg s^{-1}, together a second peak at a luminosity a factor of $\sim$5 fainter (Fig. 8). We ascribe this behaviour to its well-known spectral variability between two main states, a low-hard versus a high-soft state. A transition to the soft state was indeed reported with *INTEGRAL* in middle of 2010, after a long period spent by Cyg X–1 in hard state (Jourdain, Roques & Chauvin 2014). Also, an intermediate state is known in the source (see, e.g. Rodriguez et al. 2015 and references therein). Moreover, from its CLD another feature (an ankle) is evident: an excess of hard X-ray detections above 5×10^{36} erg s^{-1}, with respect to the extrapolation of the distribution at high luminosity. Cyg X-1 is also known to show orbital modulation of the X–ray flux, hence also this kind of variability is expected to affect its CLD. Note that we used the same conversion factor from count rate to unabsorbed flux, for all sources, including Cyg X–1, although it is known that its power-law photon index, Γ, ranges from 1.4 (hard state) to 2 in the soft state, through an intermediate state with $\Gamma = 1.7$ (Grinberg et al. 2013). An in-depth investigation of the different spectral states of Cyg X–1 with *INTEGRAL* is beyond the scope of the paper and has already been performed (Grinberg et al. 2013).

Cyg X-3 is a persistent source with one of the highest $\mathrm{DC}_{18-50\,\mathrm{keV}}$ (93.5 per cent). It is the only HMXB in our Galaxy known to host a Wolf-Rayet star as a donor (van Kerkwijk et al. 1996). The nature of the compact object is still unknown (Zdziarski, Mikołajewska & Belczyński 2013), although in the literature Cyg X–3 is often discussed as a WR-BH binary system (Esposito et al. 2013). The amplitude of its hard X–ray variability is a factor of $\sim$20, at most. An orbital modulation of its X–ray flux is known, as well as its state dependence (Weng et al. 2013). Its CLD at 18–50 keV appears unimodal and peaks at 10^{37} erg s^{-1}.

SS 433 is another peculiar, unique source in our Galaxy, thought to be in an evolutionary stage with supercritical accretion onto a BH (Cherepashchuk et al. 2013). It appears as a transient source as observed by *INTEGRAL*, with a $\mathrm{DC}_{18-50\,\mathrm{keV}}$ of 15 per cent. The CLD shape is unimodal, with a median hard X–ray luminosity $L_{\mathrm{X}} \sim 8 \times 10^{35}$ erg s^{-1}.

At lower $\mathrm{DC}_{18-50\,\mathrm{keV}}$ are located the wind-fed accretor 3A 2206+543 (Wang 2013) and the symbiotic X–ray transient XTE J1743-363 (Bozzo et al. 2013). The former shows an unimodal CLD

that above 3×10^{35} erg s^{-1} can be described by a steep power-law, similar to the high luminosity part ($L_X > 4 \times 10^{36}$ erg s^{-1}) of the CLD of Vela X–1 (Paizis & Sidoli 2014). XTE J1743-363 was included in our sample of sources, although it is not an HMXB, since symbiotic binaries sometimes show flaring activity that can resemble the SFXT flares, and can be misclassified as SFXTs, before the nature of the companion is unveiled. Its long-term behaviour is peculiar: the $DC_{18-50\,keV}$ is very low, similar to many SFXTs, but the shape of its CLDs is different, much steeper than in SFXTs, and closer to the high luminosity part of CLDs of wind-fed HMXBs, like Vela X–1.

The last source in Fig. 4 is IGR J16318–4848 (Courvoisier et al. 2003), harboring a B[e] supergiant companion (Filliatre & Chaty 2004), a rare object in our Galaxy (similar to XTE J0421+56/CI Cam, Boirin et al. 2002). From the point of view of its CLD, it is similar to what displayed by the SgHMXBs. Also its CLD skewness and median luminosity fits well within the anticorrelation shown by SgHMXBs (Fig 7, left panel). From this similarity, the correlation of the pulsar spin periods with the skewness (marked with a red triangle in Fig 7, right panel), allow us to predict a rotational period in IGR J16318–4848 ranging from a few hundreds to a few thousands seconds.

5.2 HMXBs: hard X-rays into context of other properties

In Table 1, we have listed our results on HMXBs from the *INTEGRAL* archive, while in Table 2 some properties of the sample are reported (distance, orbital period and eccentricity, pulsar spin period), together with information about the soft X–ray fluxes (see Section 4), minimum and maximum values in the energy band 1-10 keV, and their ratio ($DR_{1-10\,keV}$).

The second aim of our investigation is to put our long-term *INTEGRAL* results into context with the overall known source properties and to characterize the different HMXB phenomenology from the point of view of time-integrated quantities. Although the variable of time is lost, we gain a global, wider, view of the whole behaviour of our sample.

There are two quantities that have been often used in the literature to characterize SFXTs with respect to other SgHMXBs: the dynamic range at soft X–rays ($DR_{1-10\,keV} = F_{max}/F_{min}$) and the source duty cycle at 18–50 keV ($DC_{18-50\,keV}$, Sidoli 2017). The former energy band choice is due to the fact that instruments observing the sky in the soft X–rays are much more sensitive than in the hard X–rays, reaching the true quiescence of these objects (10^{32} erg s^{-1}, e.g. in't Zand 2005). The latter is because SFXTs were discovered by *INTEGRAL* (Sguera et al. 2005; Negueruela et al. 2006), and IBIS/ISGRI can work as a sort of high-pass filter, catching bright and short flares.

5.2.1 *Source DC* $_{18-50\,keV}$ *and DR* $_{1-10\,keV}$

We have investigated the $DC_{18-50\,keV}$ and the $DR_{1-10\,keV}$ for all sources in our sample, to enable a full characterization of the three types of HMXBs. In Fig. 9, we plot the cumulative distribution of source $DC_{18-50\,keV}$ (considering SgHMXBs, SFXTs, and Be/XRBs) and then for the three sub-classes, separately. This plot clearly demonstrates that SFXTs show a flaring activity for less than 5 per cent of the time, while the great majority of the SgHMXBs cluster around much higher $DC_{18-50\,keV}$ (SgHMXBs include persistent or almost persistent sources). However a few SgHMXBs exist that show a very low $DC_{18-50\,keV}$, suggesting that some of them are truly transient systems, probably SFXTs mis-classified as more 'standard' supergiant systems (IGR J16207–5129, IGR J16393–4643, IGR J18027–2016, and IGR J18214–1318). Alternatively, they are faint sources (probably because of their large distance), just under the sensitivity threshold of the instrument, that rarely underwent some short flaring activity, on a timescale of ∼2 ks. Be/XRBs cover a wide range of values, from an almost persistent behaviour (∼77 per cent, in X Per), through a very frequent duty cycle around 10 per cent displayed by several transient Be sources, down to very low values of ∼0.1 per cent (RX J0146.9+6121, AX J1820.5–1434, XTE J1543–568, and AX J1749.1–2733).

We found an ample range of values also for the $DR_{1-10\,keV}$ (Fig. 10), covering six orders of magnitude. The most extreme transients are among the SFXTs (IGR J17544-2619) and the Be systems (EXO 0331+530), while when looking at the global distribution, a gap is apparent around $DR_{1-10\,keV} = 100$, a value that might be used as a threshold distinguishing (almost) persistent from transient sources. Again, we unveil an overlapping region of dynamic ranges where some members of the SgHMXB class show a larger variability than the bulk of the class ($DR_{1-10\,keV} > 100$ in IGR J18027-2016, H1907+097 and IGR J19140+0951). On the contrary, the SFXT IGR J16465-4507 displays a low $DR_{1-10\,keV}$ of ∼38. The visual inspection of the cumulative distribution of $DR_{1-10\,keV}$ in SFXTs reveals a power-law-like shape. Therefore, it is simple to draw apart both the extreme values of IGR J16465–4507 (overlapping with SgHMXB) and of IGR J17544–2619. In this latter source, a different physical mechanism might have produced a very high luminosity (i.e. the formation of a transient accretion disc; Romano et al. 2015). In Be/XRBs, a large range of $DR_{1-10\,keV}$ is covered, demonstrating that the sub-class of Be sources includes many different X–ray behaviours, with no preferred variability amplitude.

There is no correlation between the $DC_{18-50\,keV}$ and the source distance (Fig. 11, left-hand panel), implying that extreme transient sources (like SFXTs) cannot be explained as SgHMXBs located at larger distances. In the right-hand panel of the same figure, the dependence of the source dynamic range with the distance is displayed, showing no apparent trend.

5.2.2 *DC* $_{18-50\,keV}$ *and other source properties*

In Fig. 12, we investigate if there is a dependence of the source $DC_{18-50\,keV}$ with other properties. In the first plot ($DC_{18-50\,keV}$ versus $DR_{1-10\,keV}$), persistent and less variable sources (like most of the SgHMXBs, marked by blue dots) lie in the upper left part (high $DC_{18-50\,keV}$, low $DR_{1-10\,keV}$), while the most transient sources (SFXTs, marked by green stars), occupy the bottom, right part of the plot (low $DC_{18-50\,keV}$, high $DR_{1-10\,keV}$). This 2D plot can be considered as a way to classify a source: sources with $DR_{1-10\,keV} > 100$ can be considered transients; among them, Be/XRTs cluster in the region with $DC_{18-50\,keV} > 5$ per cent, while the others with $DC_{18-50\,keV} < 5$ per cent are SFXTs. There are some rare exceptions (the same we mentioned before in each single plot). In particular, we suggest that IGR J18027-2016, previously classified as a SgHMXB, is an SFXT, since it shows both a very low $DC_{18-50\,keV}$ (0.54 per cent) and a high $DR_{1-10\,keV}$ (375). The region of the plane characterized by $DR_{1-10\,keV} < 100$ and $DC_{18-50\,keV} < 1$ per cent, is populated by SgHMXBs and Be/XRBs in equal number (plus the SFXT IGR J16465–4507 and a symbiotic binary): the two SgHMXBs IGR J16207–5129 and IGR J16393-4643 and the Be sources 4U 1036-56 and XTE J1543-568.

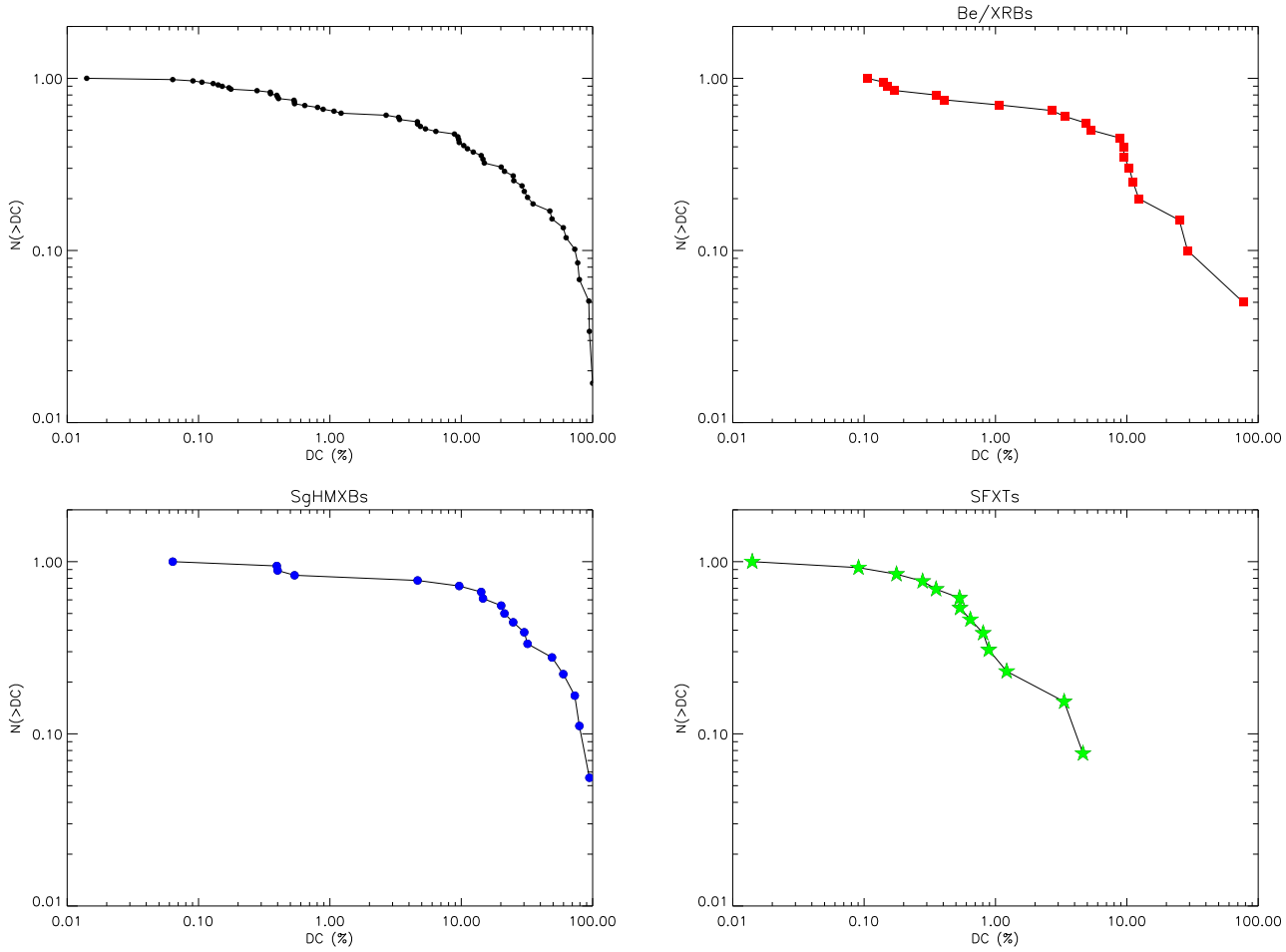

Figure 9. Normalized cumulative distributions of the 18–50 keV duty cycles, for all sources (black) and for the three sub-classes of Be/XRBs (red), SgHMXBs (blue), and SFXTs (green).

Interestingly, the peculiar source 3A 2206+543 (marked by the empty triangle at the location $DC_{18-50\,keV} = 7$ per cent and $DR_{1-10\,keV} \sim 100$) lies just in-between the three main locii occupied by the great majority of the members of the three sub-classes, confirming its anomalous phenomenology, difficult to classify (not only in the optical, but also in X–rays).

In Fig. 12, the two plots of $DC_{18-50\,keV}$ versus the pulsar spin and the orbital periodicities is meant to enlarge the transient versus persistent phenomenology shown by the Corbet diagram (see below) also to sources where one or the other are unknown. The fourth plot with $DC_{18-50\,keV}$ versus the orbital eccentricity reveals two branches: low-eccentricity sources spanning a large range of hard X–ray activity, and sources drawing an anticorrelation that starts from the top left part of the graph with persistent SgHMXBs plus the low-eccentricity, Be system X Per, to the bottom right zone, occupied by two SFXTs with the most eccentric orbits (IGR J08408–4503 and IGR J11215-5952). This suggests that the orbital eccentricity might play a role in producing transient X–ray emission in some HMXBs.

5.2.3 *Orbital geometry and pulsar spin period*

In Fig. 13, we display the so-called Corbet diagram (Corbet 1986) for our sample, where the pulsar spin period is plotted versus the orbital period of the system. The segregation of different source types is well known (Corbet 1986), together with the more recent findings that SFXTs appear to bridge the two locii where SgHMXBs and Be/XRBs are clustered (Sidoli 2017). However note that, among SFXTs, the spin period of IGR J17544–2619 (i.e. 71 s) needs a confirmation, since it was derived with a collimator (*RXTE*/PCA), so it is possible that pulsed X-rays actually come from a different transient source within the field of view. The three RLO-systems are shown in the bottom left region of the plot (LMC X–4, SMC X–1, and Cen X–3).

In the left panel of Fig. 14, we plot the source eccentricity against the orbital period, obtaining two trends: for the large majority of HMXBs, the longer the period, the more eccentric the orbit; there are however four low-eccentric Be/XRBs with orbital periods longer than 20 days (starting from the shorter orbital period, they are 4U 1901+03, KS 1947+300, XTE J1543–568 and X Per). This plot was previously investigated in detail by Townsend et al. (2011) on a larger sample of HMXBs (also including a few SMC pulsars), so we will not discuss this further, but we remind here the arguments put forward by these authors to explain the two trends: first of all, the low-eccentricity, wide-orbit, Be systems represent a separate population of Be/XRBs where the NS experienced a smaller natal kick with the first supernova explosion than the other, more eccentric, Be/XRBs (Pfahl et al. 2002). Second, the significant

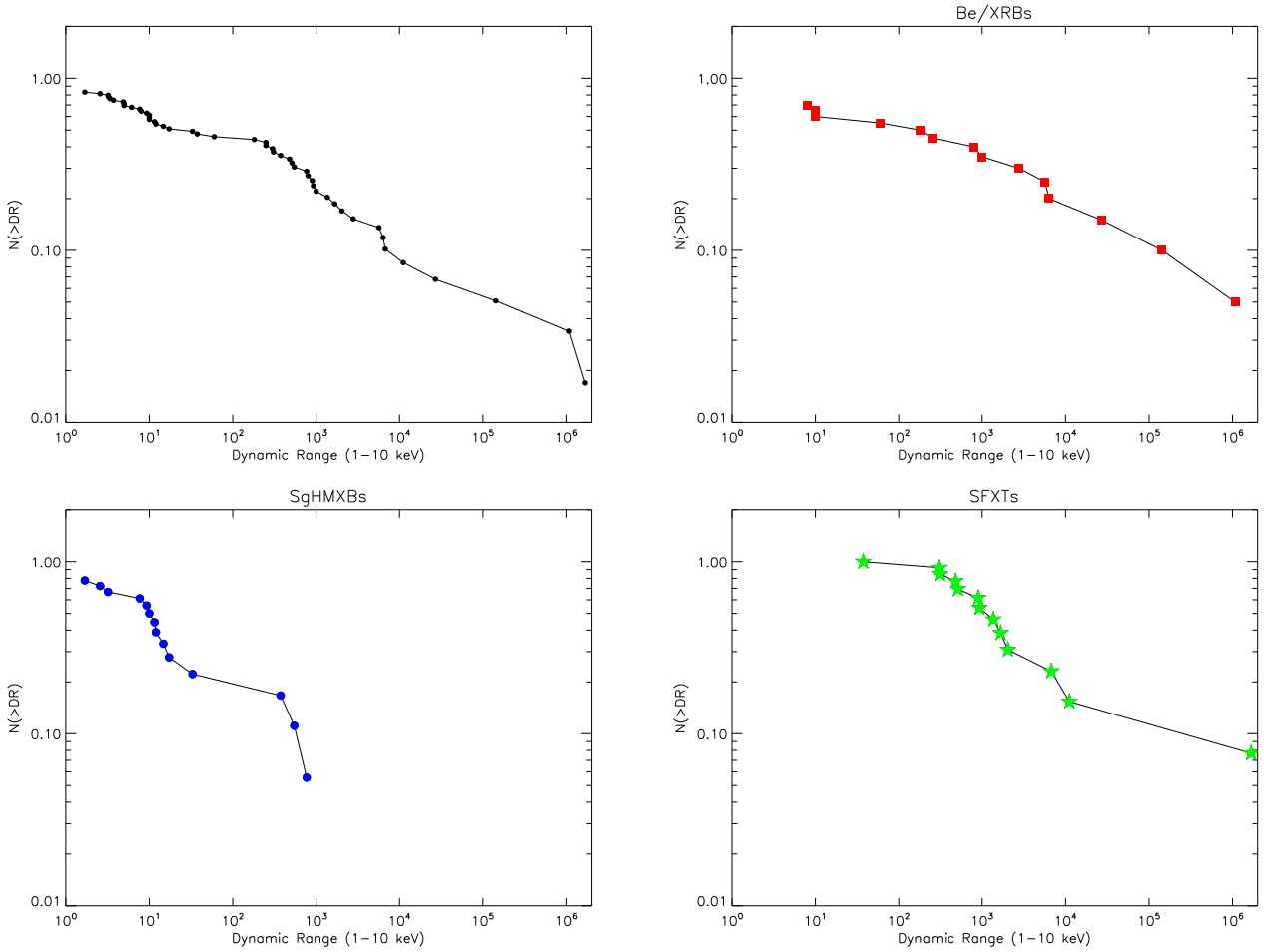

Figure 10. Normalized cumulative distributions of the 1–10 keV dynamic ranges, for all sources (black) and for the three sub-classes of Be/XRBs (red), SgHMXBs (blue), and SFXTs (green).

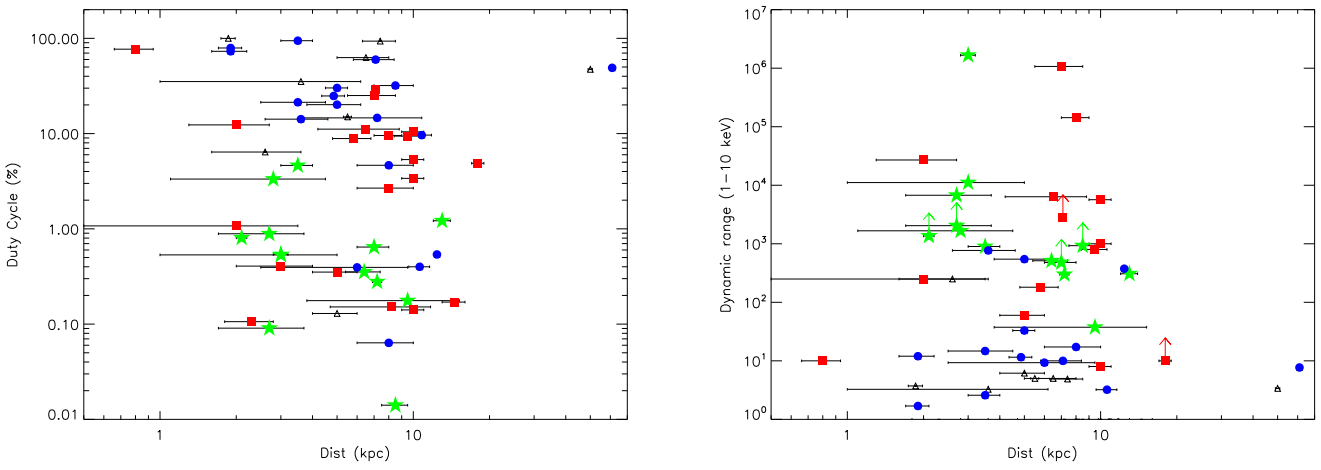

Figure 11. Dependence of the hard X-ray duty cycles (left-hand panel) and of the soft X–ray dynamic ranges (right-hand panel) with the source distance. Error bars indicate the uncertainty on the source distances, as reported in Table 2. When Table 2 does not list any uncertainty (because it is not reported in the literature), we assumed ±1 kpc. Green stars mark SFXTs, blue circles indicate SgHMXBs, red squares Be/XRBs; empty triangles mark sources that do not belong to these three subclasses and are listed in Table 2 as 'giant HMXBs', 'other HMXBs' and the 'symbiotic binary'.

correlation of eccentricity with the period in all other HMXBs is actually made of two separate sub-classes, the supergiant (at lower orbital periods) and the Be binaries (at higher orbital periods), as is also evident in our graph. Townsend et al. (2011) suggested that this latter correlation, though significant taken as a whole, might be simply explained by the superposition of the two sub-classes

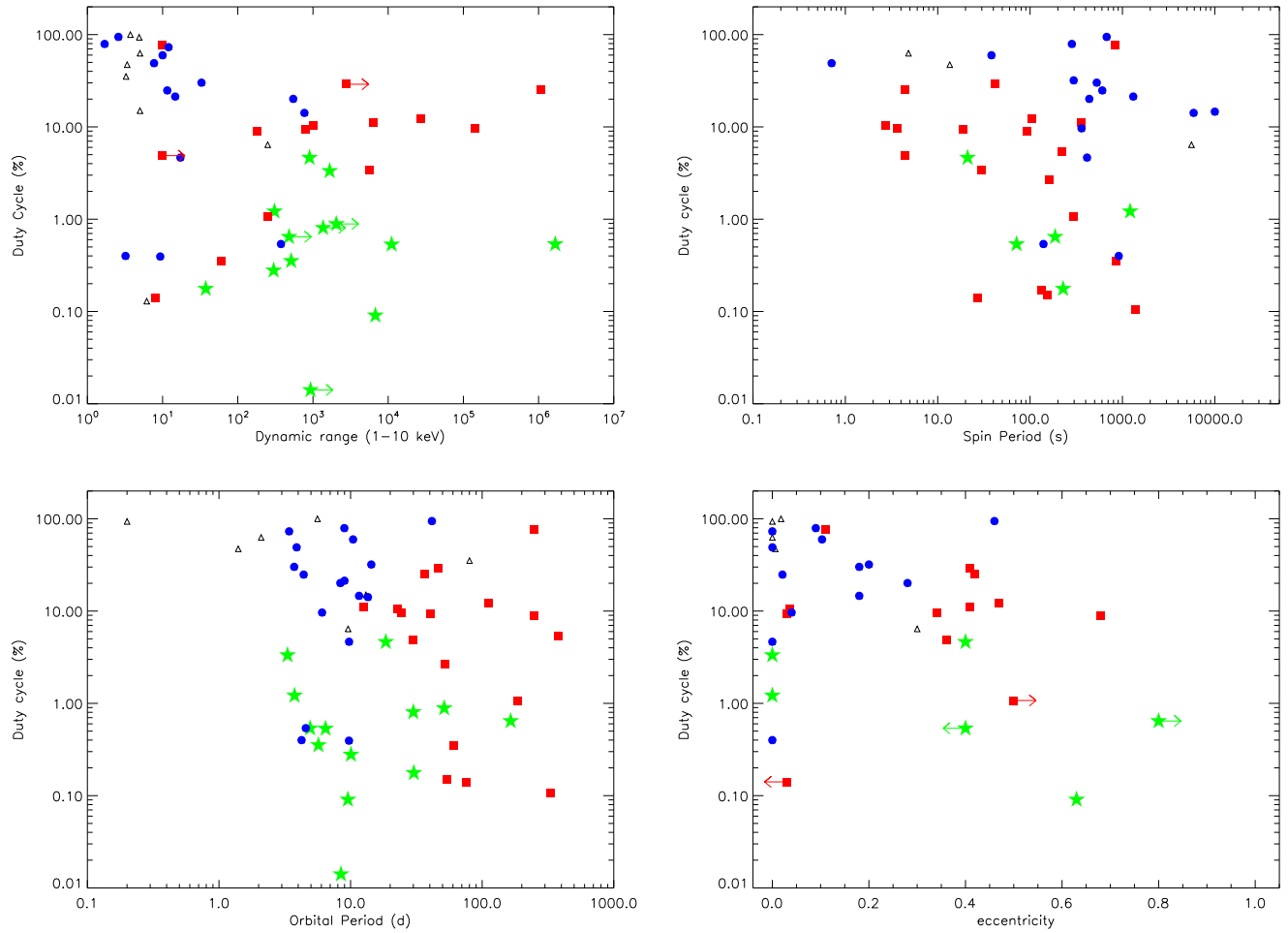

Figure 12. Properties of the sources in our sample, presented in Tables 1 and 2. The meaning of the symbols is the same as in Fig. 11. Arrows mark lower or upper limits (according to Table 2).

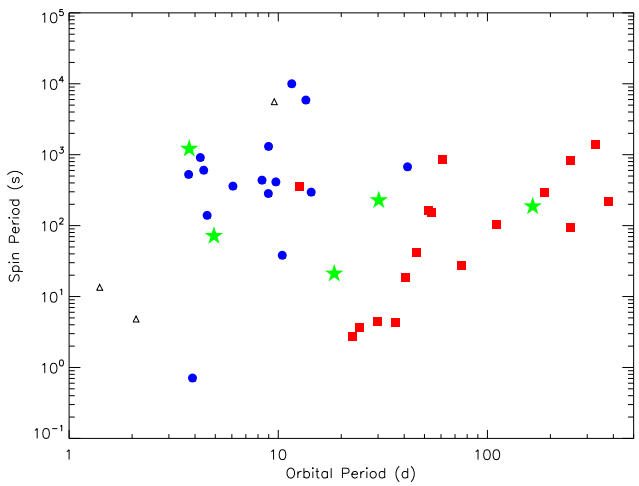

Figure 13. Pulsar rotational period versus orbital period (the so-called Corbet diagram) is shown for the HMXBs in our sample. The meaning of the symbols is the same as in Fig. 11.

(SgHMXBs and Be/XRBs) lying in two different regions of this parameter space. However, it is important to note a new remarkable finding in our version of this plot: the presence of the SFXTs (not considered by Townsend et al. 2011): although the eccentricity of two SFXTs (at $e \sim 0.4$) are quite uncertain (and only derived from the amplitude of their X-ray orbital modulation), the eccentricities (and orbital periods) of the most eccentric SFXTs IGR J08408-4503 ($e = 0.63 \pm 0.03$, $P_{\rm orb} = 9.5436 \pm 0.0002$, Gamen et al. 2015) and IGR J11215-5952 ($P_{\rm orb} = 164.6$ days, Sidoli et al. 2007; Romano et al. 2009; $e > 0.8$, Lorenzo et al. 2014) appear better determined. This allows HMXBs with supergiant companions to overlap with Be systems at large eccentricities and orbital periods.

The plane of the orbital eccentricity versus the pulsar spin period is more complex (Fig. 14, right panel). In order to discuss this plot, for the sake of clarity, we distinguish three different regions. The eccentricity e $\sim$ 0.3 seems to divide the plot into two main regions. The upper part is populated by the more transient systems (Be/XRTs and SFXTs) plus the SgHMXB GX 301–2, while the region with e $<$ 0.3 can be divided into two more parts, depending on the spin period (around $P_{\rm spin} = 100$ s): there are no pulsars (in our HMXB sample) with rotational periods in the range 40–200 s and low eccentricities ($e < 0.3$). Considering only the Be/XRBs, this recalls the result obtained by Knigge, Coe & Podsiadlowski (2011), on a sample of Be/XRB pulsars (including Magellanic Cloud's systems), who found that short (long) spin periods are preferentially located in low (high) eccentric binaries, and interpreted it as the

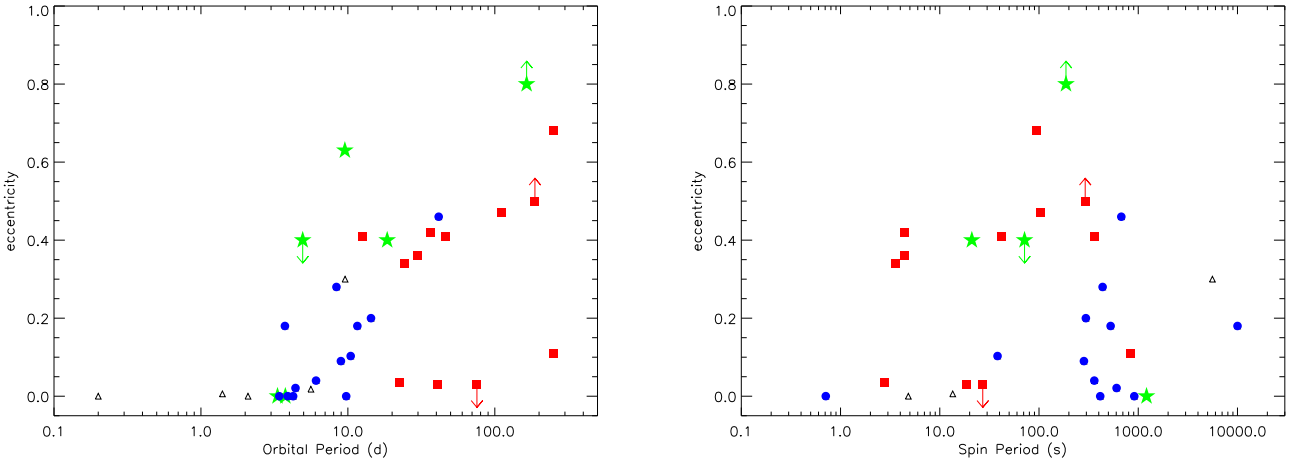

Figure 14. Properties of the sample of HMXBs, in terms of orbital eccentricity versus orbital period (*left panel*) and of eccentricity versus pulsar rotational period (*right panel*). The meaning of the symbols is the same as in Figs. 11 and 12.

results of two distinct types of NS forming supernovae. An alternative explanation was proposed by Cheng, Shao & Li (2014), who ascribed the bimodal spin distribution to different accretion modes in the Be/XRBs: shorter spin periods are present in Be/XRBs where the NS can efficiently accrete matter (producing a Type II outburst) from the warped, outer Be stellar disc, forming an accretion disc that spins up the pulsar. In Be/XRBs that are either persistent or that experience mostly Type I outburst, the accretion is suggested to be quasi-spherical and the transfer of angular momentum to the pulsar inefficient, resulting in longer spin period Be/XRB pulsars (Cheng et al. 2014). Three are the Be/XRBs in this region of the eccentricity-spin period plane: 4U 1901+03, KS 1947+300, and XTE J1543-568. This warping mechanism might explain why these low-eccentric Be/XRBs do show outbursts, instead of being persistent (like X Per): in the scenario proposed by Cheng et al. (2014) they might display the right combination of values for their eccentricity and orbital periods (see Fig. 4 in Cheng et al. 2014). The lower-right region of this plane (long spin periods and low-eccentric orbits) is occupied by wind-fed SgHMXBs (plus X Per, one SFXT and the peculiar wind accretor 3A 2206+543), where the wind accretion is unable to efficiently spin up the pulsar. Systems with supergiant and giant companions at low eccentricities and spin period shorter than 40 s, can be explained by disc accretion: these sources are the three RLO-systems together with OAO 1657–415.

5.2.4 *Minimum and maximum luminosity (1–10 keV)*

In Fig. 15, we show the dependence of the soft X–ray properties with the hard X–ray duty cycle and other quantities like the spin period and the orbital geometry. There is no apparent correlation between the $DC_{18-50\,keV}$ and the maximum soft X–ray luminosity (first upper panel), while it seems that (although with a large scatter) the lower the $DC_{18-50\,keV}$, the lower the minimum soft X–ray luminosity (second upper panel). The third panel indicates that accreting pulsars with shorter rotational periods avoid low values of their maximum luminosities (e.g. Stella et al. 1986). Although we do not plot here necessarily the X–ray luminosity of the observations where a spin period was measured, we can ascribe this trend to the on-set of the propeller effect (the solid line is drawn from equation 3). The same trend is not present (and we do not show it here) when the minimum soft X–ray luminosity is plotted against the spin period, since for X-ray transients it is taken from quiescence. In the forth panel we show the dependence of the minimum soft X–ray luminosity from the orbital eccentricity, where we found that in more eccentric systems a lower luminosity level can be reached, because the NS can orbit farther away from the donor. In the bottom panels of Fig. 15 we show, for completeness, maximum and minimum soft X–ray luminosities versus the orbital period. In these graphs, the sub-classes cluster in different regions, reflecting the trend of the Corbet diagram (that is, persistent SgHMXBs have shorter orbital period than Be/XRBs, while SFXTs bridge the two regions).

5.2.5 *Average hard X-ray luminosity*

In Fig. 16, we investigate the behaviour of the average luminosity (18–50 keV) against the source duty cycle and other source properties. In the first panel, three types of HMXBs lie in three different regions of the plane $DC_{18-50\,keV}$—L_X, with the SgHMXBs on the right, the SFXTs on the left (low duty cycles but average luminosities in outburst similar to the classical SgHMXBs), and most of the Be/XRTs showing higher average luminosities (in outburst) and intermediate duty cycles (around 10 per cent). This suggests another way to distinguish the three kinds of HMXBs from the hard X-rays properties (see below, when discussing about the source dynamic range).

In Fig. 16, the plot of the average luminosity (18–50 keV) against the orbital period shows an anticorrelation. However, it is important to remind that for transient sources (both Be and SFXTs), the averange luminosity plotted here is the average value during outbursts, as observed by *INTEGRAL*. It is known that persistent, wind-fed, SgHMXBs hosting NSs show a trend of L_X with the orbital period (Stella et al. 1986; Bhadkamkar & Ghosh 2012; Lutovinov et al. 2013, and references therein), as $L_X \propto P_{orb}^{-4/3}$. In particular, Lutovinov et al. (2013) proposed a model that permitted them to obtain an allowed region in the plane P_{orb}–L_X for a NS accreting from the wind of a supergiant. The most luminous, short period, SgHMXBs do not fit their model, being powered by RLO. We overplot here also the Be/XRBs: among them, the three low luminosity, long-period, systems (X Per, H 1145–619, and RX J0146.9+6121) seem to follow the same anticorrelation as supergiant systems. This can be explained by a similar accretion mechanism (from the polar wind of their Be companions, instead from the Be decretion disc). The other Be systems (transient ones) do not follow the same trend as

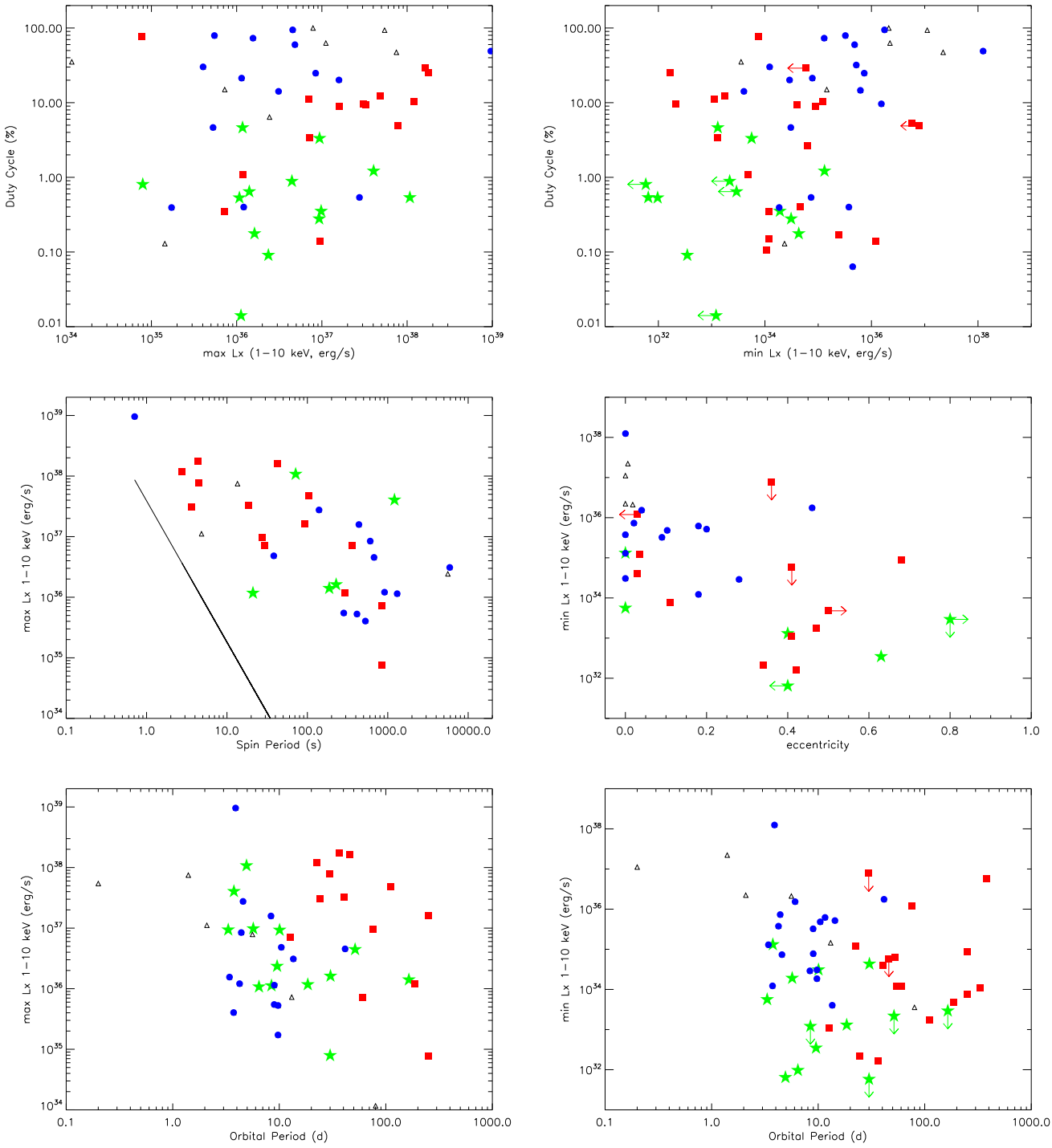

Figure 15. Properties of the sources in our sample, presented in Tables 1 and 2. The meaning of the symbols is the same as in Figs. 11 and 12. In the plot of the maximum luminosity (1–10 keV) against the spin period, the minimum luminosity before the on-set of the propeller effect is drawn (solid line), following equation (3) (assuming an NS magnetic field of 10^{12} G and $\xi = 1$).

supergiant systems, since they accrete from completely different winds (the Be decretion disc), forming, in most cases, an accretion disc around the NS. The last panels in Fig. 16 reports on the behavior of the hard X–ray average luminosity with the orbital eccentricity (on the left) and with the pulsar spin period (on the right). There is no strong correlation between luminosity and orbital eccentricity (note that for transient sources the luminosity plotted here is in outburst). The forth graph in Fig. 16 indicates an anticorrelation, the hard X–ray analogue of the one already discussed about the soft X–ray, maximum, luminosity (Stella et al. 1986). Moreover, it confirms what found by Cheng et al. (2014) in Be/XRBs, where systems with spin period shorter than 40 s show more luminous

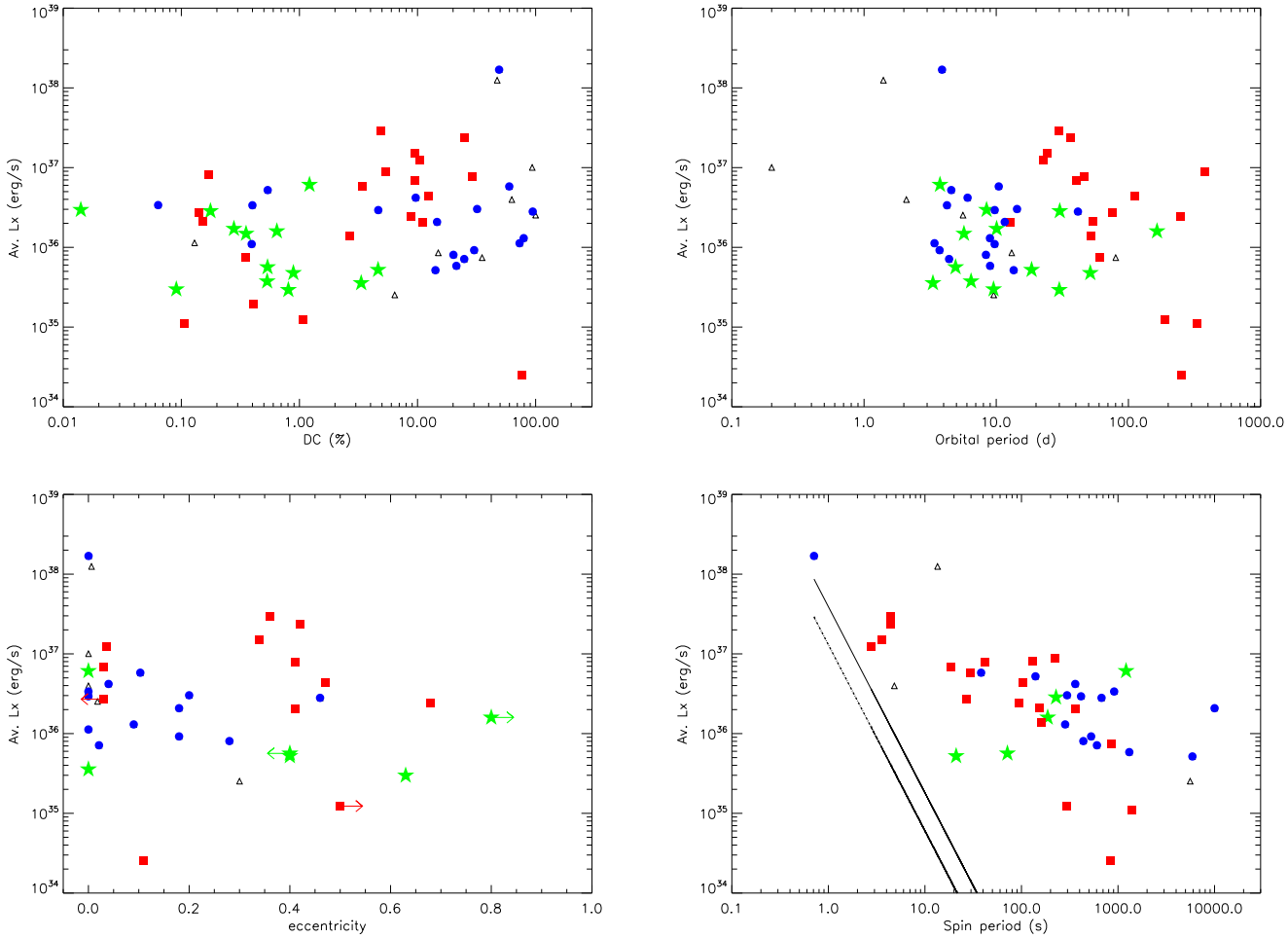

Figure 16. Properties of the sources in our sample, presented in Tables 1 and 2. The meaning of the symbols is the same as in Figs. 11 and 12. The average luminosity is at hard X–rays (18–50 keV). In the last panel, where we have plotted the average luminosity versus the spin period, the thin black line marks the minimum luminosity before the on-set of the propeller effect, following equation (3), and assuming an NS magnetic field of 10^{12} G and $\xi = 1$ (solid line). The thicker line is the same, but divided by a factor of three (assumed to be a realistic conversion factor between bolometric and 18–50 keV luminosity, see the text for details).

(Type II) outbursts than other Be/XRBs. This appears to be a confirmation of the warping mechanism, suggested to produce the giant outbursts in Be sources.

We note here that Lutovinov et al. (2013) studied the properties of the population of persistent HMXBs in the Milky Way with *INTEGRAL*, investigating their luminosity function and the spatial density distribution over the Galaxy. The authors used the 9 year *INTEGRAL* Galactic plane survey by Krivonos et al. (2012), focusing only on the persistent, wind-fed, SgHMXBs. On one side, this resulted in a sample that does not include all the transient HMXBs studied here, but on the other, given the different aims of the two works, their flux-limited sample had a sensitivity that is about one order of magnitude better than ours ($F > 10^{-11}$ erg cm^{-2} s^{-1} compared with a few 10^{-10} erg cm^{-2} s^{-1} for our *INTEGRAL* survey). In this respect, our sample of persistent wind-fed, accreting SgHMXBs with neutron stars represents a sub-sample of the HMXBs studied by Lutovinov et al. (2013).

5.2.6 *DR* $_{1-10\,\mathrm{keV}}$ *and other source properties*

In Fig. 17, we show the behaviour of the variability amplitude in soft X–rays ($\mathrm{DR}_{1-10\,\mathrm{keV}}$) depending on other source properties. The dependence of $\mathrm{DR}_{1-10\,\mathrm{keV}}$ from the spin period appears twofold: sources with a very low variabiliy are the RLO systems (SMC X–1, in blue; Cen X–3 and LMC X–4, marked by empty triangles), together with the low-eccentric Be/XRB XTE J1543–568 and the SgHMXB OAO1657–415 (that alternates disc to wind accretion). All other systems seem to show an anticorrelation with the pulsar rotational period (although note that the spin period of the SFXT IGR J17544-2619, ∼71 s, is uncertain). The largest range of variability is shown by sources with a significant orbital eccentricity, while for what concerns the orbital period there is no evidence for a trend, as a whole. However, different sub-classes occupy different regions of the $\mathrm{DR}_{1-10\,\mathrm{keV}}$–$P_{\mathrm{orb}}$ plane: this simply reflects the fact that, already mentioned before, most SgHMXBs have shorter orbital periods than Be/XRBs, while ∼40 per cent of SFXTs have orbital periods larger than 10 days, and overlap with both regions. When the average hard X–ray luminosity is plotted against the $\mathrm{DR}_{1-10\,\mathrm{keV}}$, the SgHMXBs are the less variable sources, with an average luminosity $\sim 10^{36}$ erg s^{-1}, while the transient ones, with a dynamic range larger than 10^3, divide into two completely different regions: the less luminous SFXTs (with an average hard X-ray luminosity in

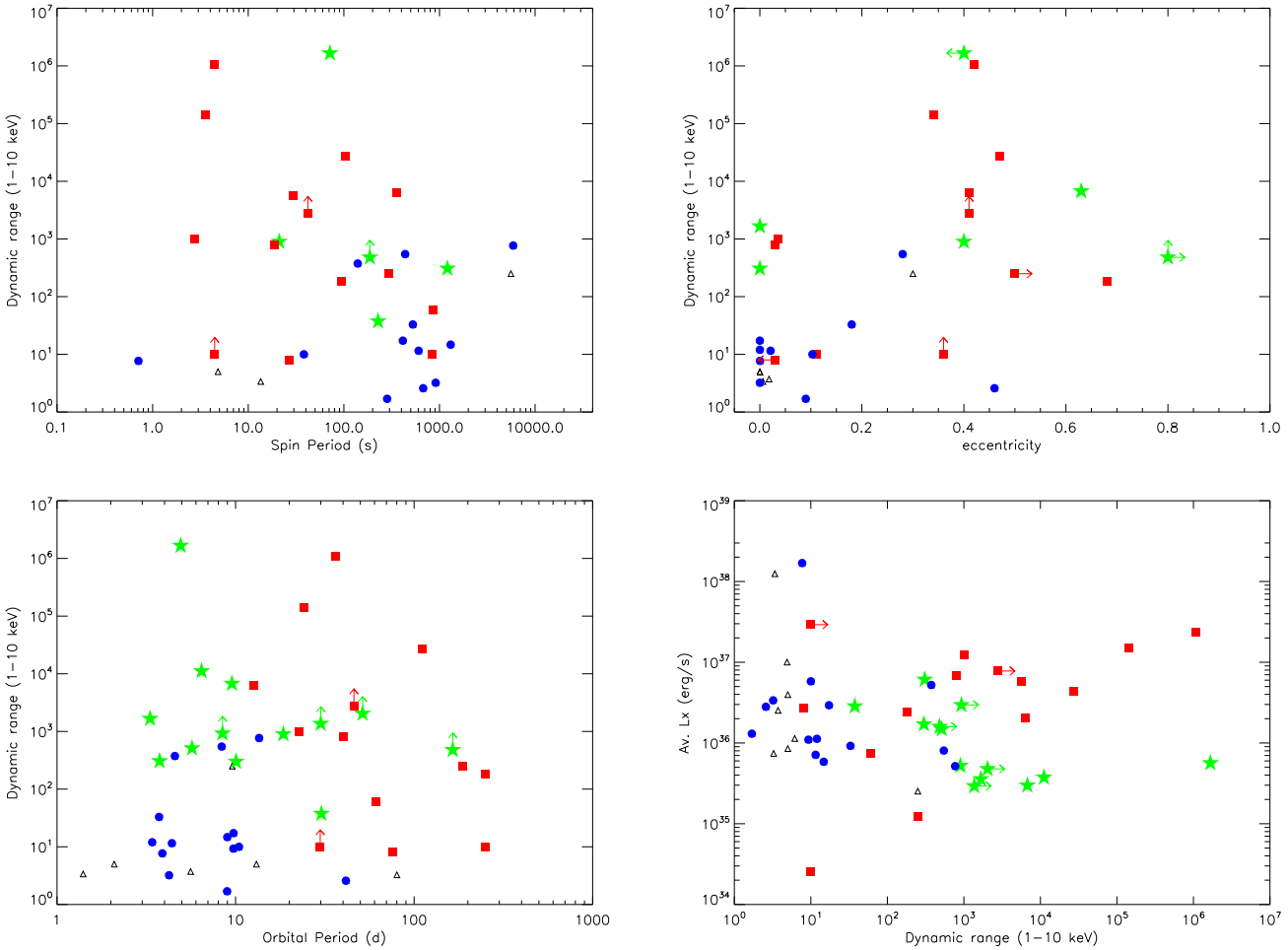

Figure 17. Properties of the sources in our sample, presented in Table 1 and Table 2. The meaning of the symbols is the same as in Figs 11 and 12.

outburst around $\sim 5 \times 10^{35}$ erg s^{-1}), whereas the Be/XRBs display luminosities higher than 10^{36} erg s^{-1} (note that these luminosities are average values, while during Type II outbursts they reach much larger values). Once again, the average luminosity appears a good indicator of the sub-class of HMXBs, for a range of high $DR_{1-10\,keV}$. Other less variable (low-eccentricity, like X Per) Be systems overlap with SgHMXBs.

5.2.7 *A global view of HMXBs*

In summary, we are now able to obtain an overview of the HMXB sample reported in this paper, from the inspection of both Figs 12 and 16 (first panels), where the three characterizing quantities of the source duty cycle $DC_{18-50\,keV}$, the average hard X-ray luminosity (in outburst, for transient sources) and the soft X–ray dynamic range, $DR_{1-10\,keV}$ are reported.

We can characterize the global behaviour of the different sub-classes, as follows:

(i) supergiant (not RLO) HMXBs show low $DR_{1-10\,keV}$ (< 40), low average X–ray luminosity ($\sim 10^{36}$ erg s^{-1}), high source duty cycles ($DC_{18-50\,keV} > 10$ per cent);

(ii) SFXTs show high $DR_{1-10\,keV}$ (>100), low average X–ray luminosity in outburst ($\sim 10^{36}$ erg s^{-1}), low source duty cycles ($DC_{18-50\,keV} < 5$ per cent);

(iii) Be/XRTs show high $DR_{1-10\,keV}$ (>100), high average X–ray luminosity in outburst ($\sim 10^{37}$ erg s^{-1}), intermediate source duty cycles ($DC_{18-50\,keV} \sim 10$ per cent);

A few sources do not fit in this picture: the RLO HMXBs (with $DR_{1-10\,keV} < 10$, high average X–ray luminosity - reaching the Eddington luminosity, high $DC_{18-50\,keV}$), the persistent Be system X Per and the three low-eccentric Be/XRBs; the reasons for their difference are clear and have been already discussed. However, there are also other systems that do not fit into this scheme, like the very variable SgHMXBs IGR J18214–1318, IGR J18027–2016, H 1907+097 and IGR J19140+0951. Since IGR J18027–2016 displays both a high $DR_{1-10\,keV}$ and a low $DC_{18-50\,keV}$, overlapping with the range of parameters shown by SFXTs, we propose to re-classify it as an SFXT. The source IGR J18214–1318 is detected only a few times by *INTEGRAL* and deserves further investigation, while the highly variable source IGR J19140+0951 is much more clearly characterized. It can be considered as an intermediate system between persistent SgHMXBs and SFXTs (Sidoli et al. 2016), similar to other SgHMXBs that have been already suggested in the literature as intermediate systems, as well (Doroshenko et al. 2012).

As discussed by Negueruela & Reig (2001) many years ago, there is a number of massive X–ray binaries that does not fit into the traditional division of HMXBs sub-classes. At that time, these authors referred to SgHMXBs and Be/XRBs, but we can extend this argument including SFXTs, and the intermediate systems we

found during our HMXB survey with *INTEGRAL*. This suggests that, although members of different sub-classes appear to cluster in different regions of the parameter space, a number of massive X–ray binaries display intermediate properties. This can also be due to the properties of the optical counterpart (as in the 'peculiar' wind-fed system 3A 2206+543).

6 CONCLUSIONS

We performed the analysis of 14 years of *INTEGRAL* observations (18–50 keV; bin time of 2 ks) of a sample of 58 HMXBs belonging to different sub-classes (SgHMXBs, SFXTs, Be/XRBs, plus a few systems which do not fit into these three types). This *INTEGRAL*-driven sample represents about a half of the total number of HMXBs in our Galaxy (Liu et al. 2006). We extracted integrated quantities (where the temporal information is lost) from this long-term dataset, to obtain an overall, representative and quantitative view of their phenomenology at hard X–rays.

Then, we collected from the literature the published values for the source properties (distance, orbital period and eccentricity, pulsar spin period) together with their minimum and maximum flux (1–10 keV), from which we have calculated their ratio. This led to the compilation of an updated catalogue of the dynamic ranges at soft X–rays for the HMXBs in our sample. We used all this information to characterize the sources and to disentangle between the properties of each sub-class.

The main results of our investigation can be summarized as follows:

(i) We built the long-term hard X-ray CLDs of HMXBs, from which it is possible to quantify, for each source, the per centage of time spent in different luminosity states, the limiting luminosity (18–50 keV), the duty cycle of their activity $DC_{18-50\,keV}$ (transient versus persistent behaviour), the variability amplitude when observed by *INTEGRAL*. Moreover:

(a) the CLDs show different shapes in the three types of massive X–ray binaries: power-law-like in SFXT flares, unimodal (and differently skewed) in supergiant and giant HMXBs hosting NSs (included RLO systems), multi-modal in BeXRTs (where the existence of different kind of outbursts, Type I vs Type II, can be immediately recognized from the step-like shape of their CLD);

(b) in SgHMXBs (plus giant systems), the shape of the CLDs appears steeper for sources with high $DC_{18-50\,keV}$ and high median luminosity, and flatter at lower $DC_{18-50\,keV}$ and lower luminosity. In fact, the skewness of the luminosity distributions shows an anti-correlation with the median luminosity and a correlation with the spin period, with the fastest SgHMXB pulsars residing in the most luminous sources, where the luminosity distribution is more symmetric and peaked. This is likely due to disc-fed versus wind-fed accretion. A by-product of this investigation is that the SgB[e] IGR J16318-4545 shows a CLD similar to wind-fed SgHMXBs.

(ii) We found that the members of the three sub-classes (SFXTs, SgHMXBs and Be/XRTs) tend to cluster around different regions defined by the following parameters: $DR_{1-10\,keV}$, $DC_{18-50\,keV}$, average 18–50 keV luminosity (in outburst for transient sources). In particular:

(a) supergiant (not RLO) HMXBs show: $DR_{1-10\,keV} < 40$, $DC_{18-50\,keV} > 10$ per cent and $L_{18-50\,keV} \sim 10^{36}$ erg s^{-1}

(b) SFXTs show: $DR_{1-10\,keV} > 100$, $DC_{18-50\,keV} < 5$ per cent and low average X–ray luminosity during flares around $L_{18-50\,keV} \sim 10^{36}$ erg s^{-1}

(c) Be/XRTs show: $DR_{1-10\,keV} > 100$, $DC_{18-50\,keV} \sim 10$ per cent and a high average X–ray luminosity in outburst around $L_{18-50\,keV} \sim 10^{37}$ erg s^{-1}

We note however that one of the results of the present study is that a number of sources shows intermediate properties, suggesting smoother edges (gradual transitions?) between the three currently known HMXBs sub-classes. With the term 'transition' we do not allude to any evolutionary meaning, here. For instance, some sources classified in the literature as SgHMXBs appear to overlap with SFXTs, showing low $DC_{18-50\,keV}$ and high $DR_{1-10\,keV}$ (IGR J18027-2016 is a striking example), suggesting a more appropriate re-classification. There are also some classical systems, like the SgHMXBs GX 301-2 or H 1907+097, that show peculiar properties with respect to SgHMXBs (as already reported in the literature). More examples are discussed in Section 5.

(iii) Albeit the *INTEGRAL*-driven source sample, we would like to note here that in the plot of the eccentricity versus the orbital period (already discussed in previous literature), we were able to add the values of some SFXTs, allowing supergiant systems to extend at larger eccentricities and orbital periods.

(iv) We performed a thorough research in the literature and compiled the most up to date catalogue of published properties of the HMXBs in our sample, including: distance, orbital period, eccentricity, spin period, self-consistently extrapolated minimum and maximum 1–10 keV flux and dynamic range, as well as the complete list of relevant references.

In conclusion, this study about HMXBs puts together the long-term *INTEGRAL* public archive spanning 14 years, the soft X–ray fluxes collected from the literature, and other important source properties (spin periods, orbital geometries), offering an interwoven overview of these sources from an observational - bird's eye - point of view.

ACKNOWLEDGEMENTS

Based on observations with *INTEGRAL*, an ESA project with instruments and science data centre funded by ESA member states (especially the PI countries: Denmark, France, Germany, Italy, Spain, and Switzerland), Czech Republic and Poland, and with the participation of Russia and the USA. We acknowledge financial contribution from ASI/INAF n.2013-025.R1 contract and from PRIN-INAF 2014 grant 'Towards a unified picture of accretion in High Mass X-Ray Binaries' (PI Sidoli). This research has made use of the NASA's Astrophysics Data System to access the scientific literature, of the SIMBAD database, operated at CDS, Strasbourg, France, and of the software WEBPIMMS provided by the High Energy Astrophysics Science Archive Research Center (HEASARC), which is a service of the Astrophysics Science Division at NASA/GSFC and the High Energy Astrophysics Division of the Smithsonian Astrophysical Observatory. We are grateful to A.J. Bird for the useful discussions. We thank the anonymous referee for the careful reading and constructive report that greatly helped improve the manuscript.

REFERENCES

Aftab N., Islam N., Paul B., 2016, MNRAS, 463, 2032

Arnaud K. A., 1996, in Jacoby G. H., Barnes J., eds, Astronomical Data Analysis Software and Systems V Vol. 101 of Astronomical Society of the Pacific Conference Series, XSPEC: The First Ten Years. p. 17

Audley M. D., Nagase F., Mitsuda K., Angelini L., Kelley R. L., 2006, MNRAS, 367, 1147

Baade D., Rivinius T., Pigulski A., Carciofi A. BRITE Executive Science Team, 2017, in Eldridge J. J., Bray J. C., McClelland L. A. S., Xiao L., eds, The Lives and Death-Throes of Massive Stars Vol. 329 of IAU Symposium, Mass-ejection events in Be stars triggered by coupled nonradial pulsation modes. p. 384
Ballhausen R. et al., 2016, A&A, 591, A65
Ballhausen R. et al., 2017, A&A, 608, A105
Baykal A., Stark M. J., Swank J. H., 2002, ApJ, 569, 903
Becker P. A. et al., 2012, A&A, 544, A123
Bhadkamkar H., Ghosh P., 2012, ApJ, 746, 22
Bird A. J. et al., 2016, ApJS, 223, 15
Blay P., Ribó M., Negueruela I., 2009, Ap&SS, 320, 145
Bodaghee A., Tomsick J. A., Rodriguez J., Chaty S., Pottschmidt K., Walter R., 2010, ApJ, 719, 451
Bodaghee A., Tomsick J. A., Rodriguez J., James J. B., 2012, ApJ, 744, 108
Bodaghee A. et al., 2016, ApJ, 823, 146
Boirin L., Parmar A. N., Oosterbroek T., Lumb D., Orlandini M., Schartel N., 2002, A&A, 394, 205
Bonnet-Bidaud J. M., van der Klis M., 1979, A&A, 73, 90
Boon C. M. et al., 2016, MNRAS, 456, 4111
Bozzo E., Campana S., Stella L., Falanga M., Israel G., Rampy R., Smith D., Negueruela I., 2008, The Astronomer's Telegram, 1493
Bozzo E., Falanga M., Stella L., 2008, ApJ, 683, 1031
Bozzo E. et al., 2011, A&A, 531, A130
Bozzo E., Pavan L., Ferrigno C., Falanga M., Campana S., Paltani S., Stella L., Walter R., 2012, A&A, 544, A118
Bozzo E., Romano P., Ferrigno C., Campana S., Falanga M., Israel G., Walter R., Stella L., 2013, A&A, 556, A30
Bozzo E., Bernardini F., Ferrigno C., Falanga M., Romano P., Oskinova L., 2017, A&A, 608, A128
Caballero-García M. D. et al., 2016, A&A, 589, A9
Campana S., Stella L., Israel G. L., Moretti A., Parmar A. N., Orlandini M., 2002, ApJ, 580, 389
Campana S., Stella L., Mereghetti S., de Martino D., 2018, A&A, 610, A46
Chaty S., Rahoui F., 2012, ApJ, 751, 150
Cheng Z.-Q., Shao Y., Li X.-D., 2014, ApJ, 786, 128
Cherepashchuk A. M., Sunyaev R. A., Molkov S. V., Antokhina E. A., Postnov K. A., Bogomazov A. I., 2013, MNRAS, 436, 2004
Coleiro A., Chaty S., 2013, ApJ, 764, 185
Corbet R. H. D., 1986, MNRAS, 220, 1047
Courvoisier T. J.-L., Walter R., Rodriguez J., Bouchet L., Lutovinov A. A., 2003, IAU Circ., 8063
Cusumano G., Segreto A., La Parola V., Masetti N., D'Aì A., Tagliaferri G., 2013, MNRAS, 436, L74
Doroshenko V., Santangelo A., Ducci L., Klochkov D., 2012, A&A, 548, A19
Doroshenko V., Tsygankov S. S., Mushtukov A. A., Lutovinov A. A., Santangelo A., Suleimanov V. F., Poutanen J., 2017, MNRAS, 466, 2143
Ducci L., Romano P., Esposito P., Bozzo E., Krimm H. A., Vercellone S., Mangano V., Kennea J. A., 2013, A&A, 556, A72
Esposito P., Israel G. L., Sidoli L., Mapelli M., Zampieri L., Motta S. E., 2013, MNRAS, 436, 3380
Evans P. A. et al., 2014, ApJS, 210, 8
Falanga M., Bozzo E., Lutovinov A., Bonnet-Bidaud J. M., Fetisova Y., Puls J., 2015, A&A, 577, A130
Filliatre P., Chaty S., 2004, ApJ, 616, 469
Fürst F., Pottschmidt K., Kreykenbohm I., Müller S., Kühnel M., Wilms J., Rothschild R. E., 2012, A&A, 547, A2
Gamen R., Barbà R. H., Walborn N. R., Morrell N. I., Arias J. I., Maíz Apellániz J., Sota A., Alfaro E. J., 2015, A&A, 583, L4
Giménez-García A., Torrejón J. M., Eikmann W., Martínez-Núñez S., Oskinova L. M., Rodes-Roca J. J., Bernabéu G., 2015, A&A, 576, A108
Grebenev S. A., Sunyaev R. A., 2007, Astron. Lett., 33, 149
Grinberg V. et al., 2013, A&A, 554, A88
Grinberg V. et al., 2013, in Goldwurm A., Lebrun F., Winkler C., eds., Proceedings of 'An INTEGRAL view of the high energy sky (the first 10 years)' the 9th INTEGRAL Workshop, October 15-19, 2012, Paris, France, in Proceedings of Science (INTEGRAL 2012)
Hilditch R. W., Howarth I. D., Harries T. J., 2005, MNRAS, 357, 304
in't Zand J. J. M., 2005, A&A, 441, L1
in't Zand J. J. M., Corbet R. H. D., Marshall F. E., 2001, ApJ, 553, L165
Inam S. Ç., Baykal A., Beklen E., 2010, MNRAS, 403, 378
Islam N., Paul B., 2016, New A, 47, 81
Islam N., Maitra C., Pradhan P., Paul B., 2015, MNRAS, 446, 4148
Israel G. L., Esposito P., Rodríguez Castillo G. A., Sidoli L., 2016, MNRAS, 462, 4371
Iyer N., Paul B., 2017, MNRAS, 471, 355
Jain C., Paul B., Dutta A., 2009, Res. Astron. Astrophys., 9, 1303
Jaisawal G. K., Naik S., Paul B., 2013, ApJ, 779, 54
Jourdain E., Roques J. P., Chauvin M., 2014, ApJ, 789, 26
Kaper L., van der Meer A., Najarro F., 2006, A&A, 457, 595
Knigge C., Coe M. J., Podsiadlowski P., 2011, Nature, 479, 372
Kreykenbohm I. et al., 2008, A&A, 492, 511
Krivonos R., Tsygankov S., Lutovinov A., Revnivtsev M., Churazov E., Sunyaev R., 2012, A&A, 545, A27
Kuehnel M. et al., 2015, in Proceedings of 'A Synergistic View of the High Energy Sky' - 10th INTEGRAL Workshop (INTEGRAL 2014). Annapolis, MD, USA, p. 78
Kühnel M. et al., 2017, A&A, 607, A88
La Palombara N., Sidoli L., Esposito P., Tiengo A., Mereghetti S., 2009, A&A, 505, 947
Labanti C. et al., 2003, A&A, 411, L149
Lamers H. J. G. L. M., Zickgraf F.-J., de Winter D., Houziaux L., Zorec J., 1998, A&A, 340, 117
Lebrun F. et al., 2003, A&A, 411, L141
Li J., Torres D. F., Zhang S., Papitto A., Chen Y., Wang J.-M., 2012, ApJ, 761, 49
Liu Q. Z., van Paradijs J., van den Heuvel E. P. J., 2006, A&A, 455, 1165
Lorenzo J., Negueruela I., Castro N., Norton A. J., Vilardell F., Herrero A., 2014, A&A, 562, A18
Lund N., Budtz-Jørgensen C., Westergaard N. J., Brandt S., Rasmussen I. L., Hornstrup A. et al., 2003, A&A, 411, L231
Lutovinov A., Tsygankov S., Chernyakova M., 2012, MNRAS, 423, 1978
Lutovinov A. A., Revnivtsev M. G., Tsygankov S. S., Krivonos R. A., 2013, MNRAS, 431, 327
Martínez-Núñez S., Kretschmar P., Bozzo E., Oskinova L. M., Puls J., Sidoli L., Sundqvist J. O., Blay P., 2017, Space Sci. Rev.
Mas-Hesse J. M., Giménez A., Culhane J. L., Jamar C., McBreen B., Torra J., Hudec R., Fabregat J., et al., 2003, A&A, 411, L261
McCollough M. L., Corrales L., Dunham M. M., 2016, ApJ, 830, L36
Nakajima M., Mihara T., Sugizaki M., Ueno S., Tomida H., Ishikawa M., Sugawara Y., Isobe N., 2017, The Astronomer's Telegram, 10608
Negueruela I., Okazaki A. T., 2001, A&A, 369, 108
Negueruela I., Reig P., 2001, A&A, 371, 1056
Negueruela I., Reig P., Coe M. J., Fabregat J., 1998, A&A, 336, 251
Negueruela I., Okazaki A. T., Fabregat J., Coe M. J., Munari U., Tomov T., 2001, A&A, 369, 117
Negueruela I., Smith D. M., Harrison T. E., Torrejón J. M., 2006, ApJ, 638, 982
Neilsen J., Lee J. C., Nowak M. A., Dennerl K., Vrtilek S. D., 2009, ApJ, 696, 182
Okazaki A. T., Negueruela I., 2001, A&A, 377, 161
Okazaki A. T., Hayasaki K., Moritani Y., 2013, PASJ, 65, 41
Orosz J. A., McClintock J. E., Aufdenberg J. P., Remillard R. A., Reid M. J., Narayan R., Gou L., 2011, ApJ, 742, 84
Paizis A., Sidoli L., 2014, MNRAS, 439, 3439
Paizis A., Mereghetti S., Götz D., Fiorini M., Gaber M., Regni Ponzeveroni R., Sidoli L., Vercellone S., 2013, Astron. Comput., 1, 33
Paizis A., Fiorini M., Franzetti P., Mereghetti S., Regni Ponzeveroni R., Sidoli L., Gaber M., 2016, in Proceedings of the 11th INTEGRAL Conference Gamma-Ray Astrophysics in Multi-Wavelength Perspective. Amsterdam, The Netherlands, p. 17
Pfahl E., Rappaport S., Podsiadlowski P., Spruit H., 2002, ApJ, 574, 364
Piraino S. et al., 2000, A&A, 357, 501
Reig P., 2008, A&A, 489, 725

Reig P., 2011, Ap&SS, 332, 1
Reig P., Milonaki F., 2016, A&A, 594, A45
Reig P., Nespoli E., 2013, A&A, 551, A1
Reig P., Roche P., 1999, MNRAS, 306, 100
Reig P., Słowikowska A., Zezas A., Blay P., 2010, MNRAS, 401, 55
Reig P., Doroshenko V., Zezas A., 2014, MNRAS, 445, 1314
Revnivtsev M., Mereghetti S., 2015, Space Sci. Rev., 191, 293
Roberts M. S. E., Michelson P. F., Leahy D. A., Hall T. A., Finley J. P., Cominsky L. R., Srinivasan R., 2001, ApJ, 555, 967
Rodes J. J., Mihara T., Torrejón J. M., Nakahira S., Bernabéeu G., Sanjurjo G., 2017, in Serino M., Shidatsu M., Iwakiri W., Mihara T., eds, 7 years of MAXI: monitoring X-ray Transients, held 5-7 December 2016 at RIKEN, p. 159
Rodriguez J., Cabanac C., Hannikainen D. C., Beckmann V., Shaw S. E., Schultz J., 2005, A&A, 432, 235
Rodriguez J. et al., 2015, ApJ, 807, 17
Romano P., 2015, J. High Energy Astrophys., 7, 126
Romano P., Sidoli L., Mangano V., Mereghetti S., Cusumano G., 2007, A&A, 469, L5
Romano P. et al., 2008, ApJ, 680, L137
Romano P. et al., 2009, MNRAS, 399, 2021
Romano P. et al., 2015, A&A, 576, L4
Rosen S. R., Webb N. A., Watson M. G., Ballet J., Barret D., Braito V., Carrera F. J., Ceballos M. T., 2016, A&A, 590, A1
Saxton R. D., Read A. M., Esquej P., Freyberg M. J., Altieri B., Bermejo D., 2008, A&A, 480, 611
Sguera V. et al., 2005, A&A, 444, 221
Shakura N., Postnov K., 2017, in Proceedings of 'Accretion Processes in Cosmic Sources', September 5-10, 2016 , St. Petersburg
Shakura N., Postnov K., Kochetkova A., Hjalmarsdotter L., 2012, MNRAS, 420, 216
Shakura N., Postnov K., Sidoli L., Paizis A., 2014, MNRAS, 442, 2325
Shakura N. I., Postnov K. A., Kochetkova A. Y., Hjalmarsdotter L., Sidoli L., Paizis A., 2015, Astron. Rep., 59, 645
Shaw S. E., Hill A. B., Kuulkers E., Brandt S., Chenevez J., Kretschmar P., 2009, MNRAS, 393, 419
Sidoli L., 2017, in Proceedings of the XII Multifrequency Behaviour of High Energy Cosmic Sources Workshop. Palermo, Italy (MULTIF2017), id.52
Sidoli L., Romano P., Mereghetti S., Paizis A., Vercellone S., Mangano V., Götz D., 2007, A&A, 476, 1307
Sidoli L. et al., 2009, MNRAS, 397, 1528
Sidoli L., Esposito P., Ducci L., 2010, MNRAS, 409, 611
Sidoli L., Mereghetti S., Sguera V., Pizzolato F., 2012, MNRAS, 420, 554
Sidoli L. et al., 2013, MNRAS, 429, 2763
Sidoli L., Paizis A., Fürst F., Torrejón J. M., Kretschmar P., Bozzo E., Pottschmidt K., 2015, MNRAS, 447, 1299
Sidoli L., Esposito P., Motta S. E., Israel G. L., Rodríguez Castillo G. A., 2016, MNRAS, 460, 3637
Sidoli L., Paizis A., Postnov K., 2016, MNRAS, 457, 3693
Sidoli L., Tiengo A., Paizis A., Sguera V., Lotti S., Natalucci L., 2017, ApJ, 838, 133
Stella L., White N. E., Rosner R., 1986, ApJ, 308, 669
Stevens J. B., Reig P., Coe M. J., Buckley D. A. H., Fabregat J., Steele I. A., 1997, MNRAS, 288, 988
Stoyanov K. A., Zamanov R. K., Latev G. Y., Abedin A. Y., Tomov N. A., 2014, Astron. Nach., 335, 1060
Tomsick J. A., Chaty S., Rodriguez J., Walter R., Kaaret P., 2008, ApJ, 685, 1143
Tomsick J. A., Chaty S., Rodriguez J., Walter R., Kaaret P., Tovmassian G., 2009, ApJ, 694, 344
Torrejón J. M., Negueruela I., Smith D. M., Harrison T. E., 2010, A&A, 510, A61
Townsend L. J., Coe M. J., Corbet R. H. D., Hill A. B., 2011, MNRAS, 416, 1556
Tsygankov S. S., Wijnands R., Lutovinov A. A., Degenaar N., Poutanen J., 2017, MNRAS, 470, 126
Ubertini P. et al., 2003, A&A, 411, L131
van Kerkwijk M. H., Geballe T. R., King D. L., van der Klis M., van Paradijs J., 1996, A&A, 314, 521
Vedrenne G. et al., 2003, A&A, 411, L63
Walter R., Lutovinov A. A., Bozzo E., Tsygankov S. S., 2015, A&A Rev., 23, 2
Wang W., 2010, A&A, 520, A22
Wang W., 2013, in van Leeuwen J., ed., Neutron Stars and Pulsars: Challenges and Opportunities after 80 years Vol. 291 of IAU Symposium, The superslow pulsation X-ray pulsars in high mass X-ray binaries. p. 203
Weng S.-S., Zhang S.-N., Ge M.-Y., Li J., Zhang S., 2013, ApJ, 763, 34
Wilson-Hodge C. A., Cherry M. L., Case G. L., Baumgartner W. H., Beklen E., Narayana Bhat P., Briggs M. S., Camero-Arranz A., 2011, ApJ, 727, L40
Winkler C., Courvoisier T., Di Cocco G., Gehrels N., Giménez A., Grebenev S., Hermsen W., Mas-Hesse J. M. et al., 2003, A&A, 411, L1
Winkler C., Diehl R., Ubertini P., Wilms J., 2011, Space Sci. Rev., 161, 149
Zdziarski A. A., Mikołajewska J., Belczyński K., 2013, MNRAS, 429, L104

SUPPORTING INFORMATION

Supplementary data are available at *MNRAS* online.

Table 1. *INTEGRAL* IBIS/ISGRI results (18–50 keV) for our sample of HMXBs.
Table 2. Summary of the source properties extracted from the literature for the different types of HMXBs of our sample.

Please note: Oxford University Press is not responsible for the content or functionality of any supporting materials supplied by the authors. Any queries (other than missing material) should be directed to the corresponding author for the article.

This paper has been typeset from a TEX/LATEX file prepared by the author.